THE GEOLOGICAL SOCIETY OF AMERICA®

Rapid assembly and crystallization of a fossil large-volume silicic magma chamber

Michael P. Eddy[1], Samuel A. Bowring[1], Robert B. Miller[2], and Jeffrey H. Tepper[3]
[1]Department of Earth, Atmospheric and Planetary Sciences, Massachusetts Institute of Technology, Cambridge, Massachusetts 02139, USA
[2]Geology Department, San Jose State University, San Jose, California 95192, USA
[3]Geology Department, University of Puget Sound, Tacoma, Washington 98416, USA

ABSTRACT

The rates at which large volumes of eruptible, silicic (>65 wt% SiO_2) magma (magma chambers) are assembled, as well as their longevity in the upper crust, remain controversial. This controversy is due, in part, to a missing record of granitoid plutonic complexes that represent large fossil upper crustal magma chambers. We present new geologic mapping and high-precision U-Pb zircon geochronology from the Eocene Golden Horn batholith in Washington State, USA. These data reveal that the batholith was constructed as a series of sills over 739 ± 34 k.y. Topographic relief of >2 km permits volume estimates for 4 of the sills, the largest of which, a >424 km³ rapakivi granite, was emplaced over 26 ± 25 k.y. at a rate of ~0.0125 km³/yr. This rate exceeds those needed to build large, silicic magma chambers in thermal models, and we suggest that that this unit may represent the first fossil magma chamber of this type recognized in the geologic record.

INTRODUCTION

Rhyolite and dacite emplaced during supereruptions demonstrate that large volumes (>450 km³) of eruptible silicic magma can exist in the upper crust. However, the time scales over which the magma reservoirs that source these eruptions are built are controversial. Thermal models suggest that magma emplacement rates need to be >0.003–0.01 km³/yr in order to accumulate enough eruptible magma to supply a supereruption (Annen, 2009; Gelman et al., 2013). However, these rates are higher than the time-averaged rates for nearly all well-studied granitoid plutonic complexes (i.e., <0.001 km³/yr; Glazner et al., 2004). This disparity contradicts evidence that supereruptions are sourced from crystal-rich magma chambers that should be preserved in the geologic record as granitoid plutons (e.g., Bachmann et al., 2007), leading to two end-member hypotheses for magma chamber construction: (1) that long-lived magma reservoirs spend the majority of their lifetimes at low melt fraction and can differentiate to form pools of eruptible magma or be rejuvenated through new magma input (Bachmann and Bergantz, 2003, 2004), or (2) that some silicic magma chambers are assembled rapidly and exist ephemerally within the upper crust (e.g., Glazner et al., 2004).

Geochronologic studies paired with robust volume estimates for magmatic intrusions provide the most direct means of assessing magma emplacement rates and quantifying crystallization duration, but the number of such studies is limited (e.g., Matzel et al., 2006; Tappa et al., 2011; Davis et al., 2012; Leuthold et al., 2012; Frazer et al., 2014; Barboni et al., 2015). Here we present new mapping and high-precision U-Pb zircon geochronology from the Golden Horn batholith (GHB) in the North Cascades, Washington State (USA). These data show that part of the batholith was assembled rapidly and may represent a fossil large-volume (>424 km³) silicic magma chamber.

GOLDEN HORN BATHOLITH

The 307 km² Eocene GHB intrudes Mesozoic sedimentary, volcanic, and plutonic rocks near the southern end of the Coast Plutonic Complex (Fig. 1A). It is dominantly peralkaline and calc-alkaline granite and granodiorite with minor diorite. The presence of a narrow metamorphic aureole, abundant miarolitic cavities, and intrusive breccias point to emplacement within the upper crust. We estimate a depth of ~7–8 km based on compositions of GHB granite that plot near the 0.2 GPa water-saturated eutectic in the quartz-albite-orthoclase (Qz-Ab-Or) system (Fig. DR1 in the GSA Data Repository[1]) and a pressure of 0.25 ± 0.06 GPa calculated using Al-in-hornblende barometry (for methods and results, see the Data Repository).

Our geologic mapping and that of Stull (1969) split the GHB into (1) peralkaline granite; (2) hypersolvus granite; (3) rapakivi granite; (4) heterogeneous granite; (5) granodiorite; and (6) diorite (Figs. 1B and 1C; for petrographic descriptions, see the Data Repository); topographic relief of >2 km gives excellent three-dimensional control on unit geometry and shows that they form sheet-like bodies (Figs. 1B and 1C). Volumes were estimated by assuming that each sheet had a constant thickness and was tabular across its areal extent, including eroded portions where we can confidently project units across glacial valleys. (For the thicknesses and areas used for these estimates, see the Data Repository) The peralkaline and hypersolvus granites are exposed in a downdropped fault block in the southeastern part of the GHB (Fig. 1B), and we calculate volumes of 29 km³ and 54 km³, respectively, for these units. These volumes are likely minimums because they do not include any parts of these sheets that may have extended to the northwest, but are now eroded. A larger size for the hypersolvus granite is suggested by a <50-m-wide (not shown in Fig. 1B) zone of this unit exposed along the western side of the batholith. We assume that the rapakivi granite and heterogeneous granite extend under the entire areal extent of the granitoid portions of the GHB, resulting in volumes of >424 km³ and 197 km³, respectively. The volume of the rapakivi granite is a minimum estimate because the top and bottom of the sheet are not exposed within the same fault block (Fig. 1B). Volumes for the diorite and granodiorite were not estimated due to their limited exposure.

U-Pb ZIRCON GEOCHRONOLOGY

Our minimum volume estimates for the GHB provide an excellent opportunity to estimate magma emplacement rates, and we dated 15 samples using U-Pb zircon chemical abrasion–isotope dilution–thermal ionization mass spectrometry geochronology (Mattinson, 2005) with this goal in mind. (For the methods used for these analyses, see the Data Repository; measured isotopic data are in Table DR4, select zircon cathodoluminesence [CL] images are in Fig. DR3, and concordia plots are in Fig. DR6.) We use $^{206}Pb/^{238}U$ dates for all of our interpretations because this chronometer provides the most precise and accurate date for

[1]GSA Data Repository item 2016104, unit descriptions, methods and results for Al-in-hornblende barometry, zircon CL images and petrography, U-Pb geochronology methods, and Monte Carlo methods, is available online at www.geosociety.org/pubs/ft2016.htm, or on request from editing@geosociety.org or Documents Secretary, GSA, P.O. Box 9140, Boulder, CO 80301, USA.

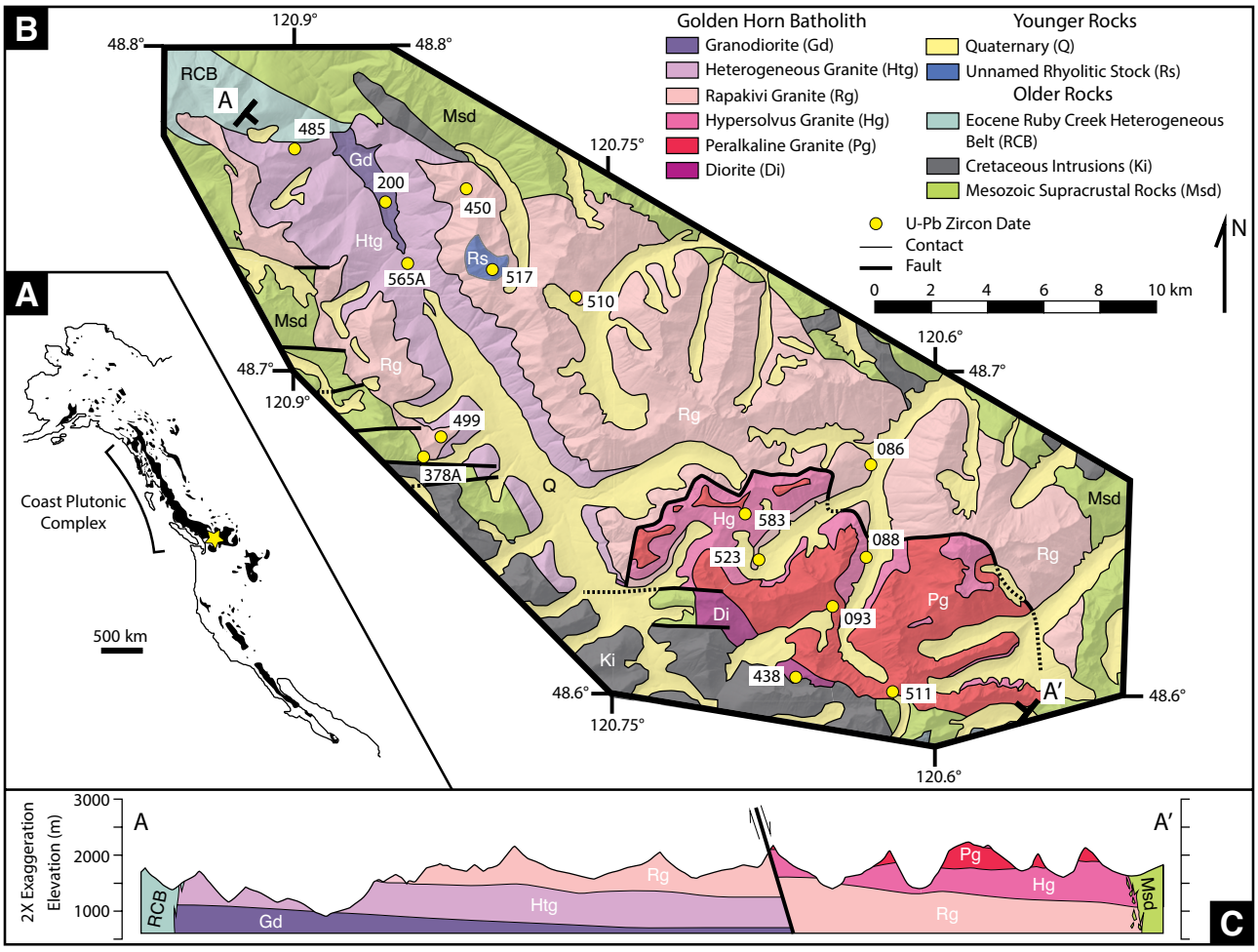

Figure 1. A: Map modified from Miller et al. (2000) showing the location of the Golden Horn batholith (GHB, yellow star) in relation to other Mesozoic and Paleogene plutonic rocks in the North American Cordillera (shown in black). B: Geologic map of the GHB. Internal contacts are based on our mapping and that of Stull (1969). External contacts are from Haugerud and Tabor (2009). The locations of samples dated by U-Pb zircon geochronology are shown with yellow circles. Sample names are abbreviated such that XXX should be read as NC-MPE-XXX. C: Cross section of the GHB along A-A′ showing the sheet-like nature of the mapped units

rocks of this age. Reported dates are corrected for initial disequilibrium in the ^{238}U-^{206}Pb decay chain using the measured $[Th/U]_{zircon}$ and the mean ratio of zircon/melt partition coefficients for Th and U ($f_{ThU} = 0.138$) from high-SiO_2 rhyolites erupted from the Yellowstone caldera (Stelten et al., 2015). The 2σ variability in the mean square weighted deviation (MSWD; Wendt and Carl, 1991) of weighted means is used to determine whether analytical uncertainty can account for the observed intrasample dispersion in zircon dates or whether it represents resolvable age differences in zircon crystallization. With the exception of a single antecrystic grain found in sample NC-MPE-485 (Fig. 2A), which is excluded from our calculations, none of the samples have resolvable age dispersion (Table 1). Therefore, we conclude that the duration of zircon crystallization within each hand sample is equal to or less than our analytical uncertainty (18–34 k.y.). Because all of the analyses used the same isotopic tracer and decay constants, all discussion of the data uses analytical uncertainty only.

The petrologic significance of zircon dates is dependent on when the melt became saturated with this mineral during its crystallization history. Early saturation can result in inherited zircons entrained from the magma's source region or antecrystic zircons that record crystallization at depth prior to transport and emplacement, leading to overestimates of the magma residence time in the upper crust (Miller et al., 2007; Barboni et al., 2015). Alternatively, late zircon saturation may lead to limited age dispersion that underestimates residence time. CL images of zircons from the GHB do not show inherited cores (Fig. DR3), and only one of the dated zircons is demonstrably antecrystic (Fig. 2A), suggesting that the majority of GHB magmas intruded at temperatures above zircon saturation (Miller et al., 2003). Furthermore, petrographic observations (Fig. DR4) demonstrate that zircon predated or cocrystallized with the major rock-forming minerals in each sample, and we consider the duration of zircon crystallization to approximate the duration of magma crystallization at the emplacement level.

The difference between the oldest and youngest dates within the GHB demonstrates that it was built over at least 739 ± 34 k.y. (Fig. 2A), starting with intrusion of the diorite and followed by downward accretion of the peralkaline granite, hypersolvus granite, rapakivi granite, and granodiorite sills. Subsequently, the heterogeneous granite intruded along the contact between the rapakivi granite and granodiorite, and a subvolcanic stock of uncertain relationship to the batholith intruded the rapakivi granite (Fig. 1B). Estimates for the duration of magmatism within individual units are reported in Figure 2A and represent the difference between the weighted mean dates of the oldest and youngest samples.

MAGMA CHAMBER CONSTRUCTION AND CRYSTALLIZATION

Magma emplacement rates were calculated assuming a constant rate of emplacement over our calculated durations. The duration magnitudes are

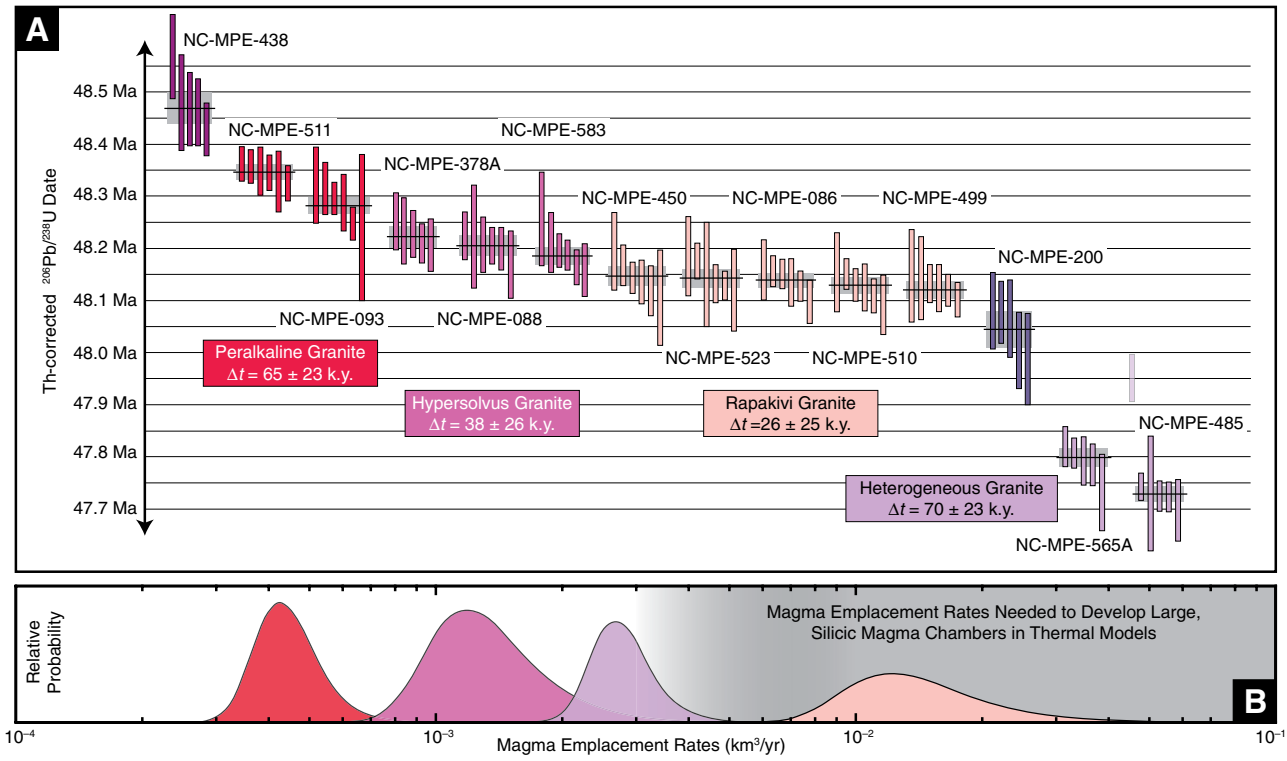

Figure 2. A: Rank order plot of Th-corrected $^{206}Pb/^{238}U$ zircon dates (bars represent 2σ analytical uncertainty) from the Golden Horn batholith (GHB). Colors correspond to map units and are the same as Figure 1B. Heavy black lines denote the weighted mean date for each sample reported with 2σ analytical uncertainty (gray boxes). For map units with more than one dated sample, we present the duration (Δ*t*) of magmatism calculated using the difference between weighted means of the oldest and youngest samples. B: Relative probability plots for magma emplacement rates within the GHB (colors as in Fig. 1B) calculated using Monte Carlo simulations (for methods, see the Data Repository [see footnote 1]). The heights of the curves are, respectively, scaled 1×, 5×, 5×, and 30× for the peralkaline, hypersolvus, heterogeneous, and rapakivi granites, to aid in comparison. The emplacement rates (>0.003–0.01 km³/yr) needed to produce large volumes of eruptible silicic magma in thermal models (Annen, 2009; Gelman et al., 2013) are shaded gray.

similar to our analytical uncertainty and lead to asymmetric probability distributions for rates calculated using Monte Carlo simulations (Fig. 2B; for methods, see the Data Repository). Given this asymmetry, we report the mode of these distributions as the best estimate for the magma emplacement rate in each unit. The peralkaline (~0.0004 km³/yr), hypersolvus (~0.0012 km³/yr), and heterogeneous granite (~0.0027 km³/yr) span the range of rates in other well-studied plutonic complexes (Fig. DR7), and distinct sample dates (Fig. 2A) and sharp internal contacts support the interpretation that these bodies never formed single, large-volume magma chambers. The rapakivi granite, however, has a calculated magma emplacement rate of 0.0125 km³/yr, exceeding the rates required for the construction of large-volume silicic magma chambers in thermal models (Fig. 2B). While it is possible that our dates for this unit do not span its complete emplacement duration, overlapping zircon dates (Fig. 2A) from five widely spaced samples (Fig. 1B) indicate that melt was simultaneously present throughout most of the sheet. Because we infer that zircon crystallization occurred over a similar interval to that of magma crystallization, we suggest that this unit represents a large fossil silicic magma chamber. The 26 ± 25 k.y. duration of magma emplacement and crystallization implies that this body was an ephemeral feature and crystallized much faster than the crystallization time scales (>100 k.y.) predicted for silicic magma reservoirs the size of the rapakivi granite at ~5–10 km (Gelman et al., 2013). The reasons for such rapid crystallization are unknown, but may include the relatively short duration of high magma emplacement rates and the evolved nature of the melt (whole-rock SiO_2 ranges from 73 to 76 wt%; Stull, 1969).

Extremely high magma emplacement rates likely trigger eruptions by generating overpressure within magma chambers (e.g., Degruyter et al., 2016), and this may explain the scarcity of rapidly assembled silicic magma chambers in the plutonic record (e.g., Glazner et al., 2004; Tappa et al., 2011). It is currently unclear whether any part of the GHB is related to an eruption. In the Chumstick strike-slip basin, ~100 km to the south of the GHB, 9 tuffs closely match the batholith in age (Eddy et al., 2016), but the geochemical data needed to assess whether they are cogenetic do not exist. Nevertheless, the discovery of extremely high magma emplacement

TABLE 1. U-Pb ZIRCON GEOCHRONOLOGY RESULTS

Sample*	Weighted mean $^{206}Pb/^{238}U$ date† (Ma)
NC-MPE-438	48.468 ± 0.030/0.037/0.064 (n = 5, MSWD = 1.84)
NC-MPE-511	48.346 ± 0.015/0.026/0.058 (n = 6, MSWD = 0.69)
NC-MPE-093	48.281 ± 0.018/0.028/0.059 (n = 6, MSWD = 1.91)
NC-MPE-378A	48.223 ± 0.021/0.030/0.060 (n = 5, MSWD = 0.54)
NC-MPE-088	48.205 ± 0.020/0.030/0.060 (n = 6, MSWD = 0.42)
NC-MPE-583	48.185 ± 0.016/0.027/0.058 (n = 6, MSWD = 1.27)
NC-MPE-450	48.146 ± 0.018/0.028/0.059 (n = 6, MSWD = 1.08)
NC-MPE-523	48.144 ± 0.017/0.027/0.058 (n = 6, MSWD = 1.33)
NC-MPE-086	48.139 ± 0.014/0.025/0.057 (n = 6, MSWD = 1.44)
NC-MPE-510	48.129 ± 0.016/0.026/0.058 (n = 6, MSWD = 1.26)
NC-MPE-499	48.120 ± 0.017/0.027/0.058 (n = 6, MSWD = 0.50)
NC-MPE-200	48.045 ± 0.034/0.041/0.066 (n = 5, MSWD = 1.33)
NC-MPE-565A	47.799 ± 0.018/0.028/0.058 (n = 5, MSWD = 1.38)
NC-MPE-485	47.729 ± 0.015/0.026/0.057 (n = 5, MSWD = 0.64)
NC-MPE-517	<47.988 ± 0.052/0.056/0.076 (n = 1, maximum age)

*GPS locations for samples are presented in Table DR4 (see footnote 1).
†Corrected for initial Th/U disequilibrium using $f_{Th/U}$ = 0.138 (Stelten et al., 2015).
Uncertainties are reported in the format ±X/Y/Z, where X is the analytical uncertainty, Y includes uncertainty in the EARTHTIME ^{205}Pb-^{235}U-^{238}U isotopic tracer (Condon et al., 2015; McLean et al., 2015), and Z includes uncertainty in the ^{238}U decay constant. MSWD—mean square of weighted deviates.

rates in the rapakivi granite of the GHB demonstrates that plutons representing rapidly assembled large-volume silicic magma chambers can be preserved in the geologic record, and we anticipate that more such fossil chambers will be discovered in the future.

CONCLUSIONS

New geologic mapping and high-precision U-Pb zircon geochronology from the Eocene GHB provide estimates of magma emplacement rates for four of six map units. The largest unit, a >424 km^3 body of rapakivi granite, was built over 26 ± 25 k.y., implying a magma emplacement rate of ~0.0125 km^3/yr. This is the highest rate documented in a granitoid pluton and exceeds the thermally modeled requirements for the development of large silicic magma chambers. We suggest that this unit represents the first fossil large-volume silicic magma chamber identified in the geologic record. The continued study and documentation of such chambers will provide unique opportunities to better understand the processes that occur within these chambers and their relationship to large eruptions.

ACKNOWLEDGMENTS

We thank B. Klein, M. Ibanez-Mejia, N. McLean, O. Jagoutz, and C. Scudder for discussions about data interpretation; A. Gregovich, D. Vassey, F. Paine, M. Carpenter, and T. LaCasse for field assistance; and E. Barry and J. Pu for laboratory assistance. This work was supported by National Science Foundation grants EAR-1118883 to Bowring, EAR-1119358 to Miller, and EAR-1119252 to Tepper. This paper benefited from insightful reviews by A. Glazner, O. Bachmann, and an anonymous reviewer, and the editorial handling of J. Spotila.

REFERENCES CITED

Annen, C., 2009, From plutons to magma chambers: Thermal constraints on the accumulation of eruptible silicic magma in the upper crust: Earth and Planetary Science Letters, v. 284, p. 409–416, doi:10.1016/j.epsl.2009.05.006.

Bachmann, O., and Bergantz, G.W., 2003, Rejuvenation of the Fish Canyon magma body: A window into the evolution of large-volume silicic magma systems: Geology, v. 31, p. 789–792, doi:10.1130/G19764.1.

Bachmann, O., and Bergantz, G.W., 2004, On the origin of crystal-poor rhyolites: Extracted from batholithic crystal mushes: Journal of Petrology, v. 45, p. 1565–1582, doi:10.1093/petrology/egh019.

Bachmann, O., Miller, C.F., and de Silva, S.L., 2007, The volcanic-plutonic connection as a stage for understanding crustal magmatism: Journal of Volcanology and Geothermal Research, v. 167, p. 1–23, doi:10.1016/j.jvolgeores.2007.08.002.

Barboni, M., Annen, C., and Schoene, B., 2015, Evaluating the construction and evolution of upper crustal magma reservoirs with coupled U/Pb zircon geochronology and thermal modeling: A case study from the Mt. Capanne pluton (Elba, Italy): Earth and Planetary Science Letters, v. 432, p. 436–448, doi:10.1016/j.epsl.2015.09.043.

Condon, D.J., Schoene, B., McLean, N.M., Bowring, S.A., and Parrish, R.R., 2015, Metrology and traceability of U-Pb isotopic dilution geochronology (EARTHTIME tracer calibration part I): Geochimica et Cosmochimica Acta, v. 164, p. 464–480, doi:10.1016/j.gca.2015.05.026.

Davis, J.W., Coleman, D.S., Gracely, J.T., Gaschnig, R., and Stearns, M., 2012, Magma accumulation rates and thermal histories of plutons of the Sierra Nevada batholith, CA: Contributions to Mineralogy and Petrology, v. 163, p. 449–465, doi:10.1007/s00410-011-0683-7.

Degruyter, W., Huber, C., Bachmann, O., Cooper, K.M., and Kent, A.J.R., 2016, Magma reservoir response to transient recharge events: The case of Santorini volcano (Greece): Geology, v. 44, p. 23–26, doi:10.1130/G37333.1.

Eddy, M.P., Bowring, S.A., Umhoefer, P.J., Miller, R.B., McLean, N.M., and Donaghy, E.E., 2016, High-resolution temporal and stratigraphic record of Siletzia's accretion and triple junction migration from nonmarine sedimentary basins in central and western Washington: Geological Society of America Bulletin, doi:10.1130/B31335.1.

Frazer, R.E., Coleman, D.S., and Mills, R.D., 2014, Zircon U-Pb geochronology of the Mount Givens Granodiorite: Implications for the genesis of large volumes of eruptible magma: Journal of Geophysical Research, v. 119, p. 2907–2924, doi:10.1002/2013JB010716.

Gelman, S.E., Gutierrez, F.J., and Bachmann, O., 2013, On the longevity of large upper crustal silicic magma reservoirs: Geology, v. 41, p. 759–762, doi:10.1130/G34241.1.

Glazner, A.F., Bartley, J.M., Coleman, D.S., Gray, W., and Taylor, R.Z., 2004, Are plutons assembled over millions of years by amalgamation from small magma chambers: GSA Today, v. 14, p. 4–11, doi:10.1130/1052-5173(2004)014<0004:APAOMO>2.0.CO;2.

Haugerud, R.A., and Tabor, R.W., 2009, Geologic map of the North Cascade range, Washington: U.S. Geological Survey Scientific Investigations Map 2940, scale 1:200,000, 52 p.

Leuthold, J., Muntener, O., Baumgartner, L.P., Putlitz, B., Ovtcharova, M., and Schaltegger, U., 2012, Time resolved construction of a bimodal laccolith (Torres del Paine, Patagonia): Earth and Planetary Science Letters, v. 325–326, p. 85–92, doi:10.1016/j.epsl.2012.01.032.

Mattinson, J.M., 2005, Zircon U-Pb chemical abrasion ("CA-TIMS") method: Combined annealing and multi-step partial dissolution analysis for improved precision and accuracy of zircon ages: Chemical Geology, v. 220, p. 47–66, doi:10.1016/j.chemgeo.2005.03.011.

Matzel, J.E.P., Bowring, S.A., and Miller, R.B., 2006, Time scales of pluton construction at differing crustal levels: Examples from the Mount Stuart and Tenpeak intrusions, North Cascades, Washington: Geological Society of America Bulletin, v. 118, p. 1412–1430, doi:10.1130/B25923.1.

McLean, N.M., Condon, D.J., Condon, B., and Bowring, S.A., 2015, Evaluating uncertainties in the calibration of isotopic reference materials and multi-element isotopic tracers (EARTHTIME tracer calibration II): Geochimica et Cosmochimica Acta, v. 164, p. 481–501, doi:10.1016/j.gca.2015.02.040.

Miller, C.F., McDowell, S.M., and Mapes, R.W., 2003, Hot and cold granites? Implications of zircon saturation temperatures and preservation of inheritance: Geology, v. 31, p. 529–532, doi:10.1130/0091-7613(2003)031<0529:HACGIO>2.0.CO;2.

Miller, J.S., Matzel, J.E.P., Miller, C.F., Burgess, S.D., and Miller, R.B., 2007, Zircon growth and recycling during the assembly of large, composite arc plutons: Journal of Volcanology and Geothermal Research, v. 167, p. 282–299, doi:10.1016/j.jvolgeores.2007.04.019.

Miller, R.B., Paterson, S.R., DeBari, S.M., and Whitney, D.L., 2000, North Cascades Cretaceous crustal section: Changing kinematics, rheology, metamorphism, pluton emplacement and petrogenesis from 0 to 40 km depth, *in* Woodsworth, G.J., et al., eds., Guidebook for geological field trips in southwestern British Columbia and northern Washington: Vancouver, Geological Association of Canada, p. 229–278.

Stelten, M.E., Cooper, K.M., Vazquez, J.A., Calvert, A.T., and Glessner, J.J.G., 2015, Mechanisms and timescales of generating eruptible rhyolitic magmas at Yellowstone caldera from zircon and sanidine geochronology and geochemistry: Journal of Petrology, v. 56, p. 1607–1642, doi:10.1093/petrology/egv047.

Stull, R.J., 1969, The geochemistry of the southeastern portion of the Golden Horn batholith, Northern Cascades, Washington [Ph.D. thesis]: Seattle, University of Washington, 127 p.

Tappa, M.J., Coleman, D.S., Mills, R.D., and Samperton, K.M., 2011, The plutonic record of a silicic ignimbrite from the Latir volcanic field, New Mexico: Geochemistry, Geophysics, Geosystems, v. 12, Q10011, doi:10.1029/2011GC003700.

Wendt, I., and Carl, C., 1991, The statistical distribution of the mean square weighted deviation: Chemical Geology, v. 86, p. 275–285, doi:10.1016/0168-9622(91)90010-T.

Manuscript received 23 December 2015
Revised manuscript received 28 February 2016
Manuscript accepted 29 February 2016

Printed in USA

SUPPLEMENT TO "RAPID ASSEMBLY AND CRYSTALLIZATION OF A FOSSIL, LARGE-VOLUME, SILICIC MAGMA CHAMBER"

Michael P. Eddy, Samuel A. Bowring, Robert B. Miller, Jeffrey H. Tepper

Lithologic Descriptions

Peralkaline granite: Misch (1965) first recognized peralkaline granite within the Golden Horn batholith (GHB) and the rock was subsequently described by Stull (1969). It forms a ~400 m thick sheet of leucocratic, medium-grained granite dominantly composed of perthite, quartz, and sodic amphiboles (riebeckite, arfvedsonite) exposed in a down-dropped fault block (72 km^2) in the southeastern portion of the batholith (Fig. 1B and 1C). The presence of dark blue sodic amphibole is diagnostic in the field. Quartz occurs as large (5-10 mm) rounded crystals and in granophyric intergrowths between large grains (Stull, 1969). Miarolitic cavities are abundant within this lithology and range from several millimeters to one meter in diameter. The cavities are filled with diverse minerals, including several unique to the GHB (Boggs, 1984). Dikes of the hypersolvus granite cut the peralkaline granite and establish a relative age relationship between the two lithologies. The normative mineralogy of the peralkaline granite plots near the 0.2 GPa H_2O-saturated eutectic in the Ab-Or-Qz system (Fig. DR1).

Hypersolvus granite: Hypersolvus granite was first mapped and described by Stull (1969). It forms two subhorizontal sheets exposed in the southeastern portion of the GHB (Fig. 1B and 1C). The first sheet is only exposed at very high elevations and remains poorly documented and undated. The second sheet is ~750 m thick and is exposed underneath the peralkaline granite. The contact between the two lithologies is sharp and marked by highly weathered hypersolvus granite (Stull, 1969), and the sheet's lower contact with the rapakivi granite appears to be gradational. The hypersolvus granite is primarily composed of perthite, quartz, biotite, and hornblende and is distinguished from the peralkaline granite based on the absence of sodic amphiboles and the presence of biotite. Miarolitic cavities are abundant. The normative mineralogy of the hypersolvus granite plots just below the 0.2 GPa H_2O-saturated eutectic in the Ab-Or-Qz system (Fig. DR1). The current areal exposure of this unit is largely restricted to the down-dropped fault block (72 km^2) in the SE of the GHB. However, a thin screen of hypersolvus granite that extends along the west side of the batholith suggests that it may have once covered a larger area. Nevertheless, we use the 72 km^2 area of the fault block to calculate a minimum volume estimate for the unit and neglect the undated upper hypersolvus sheet in our calculations.

Rapakivi granite: The rapakivi granite was described in detail by Stull (1969, 1978). It is coarse grained and dominantly composed of plagioclase, orthoclase, quartz, and biotite ± hornblende. Perthitic orthoclase mantled with plagioclase (rapakivi texture) is pervasive and is a distinguishing characteristic in the field. Enclaves are common within the rapakivi granite and range from small (<1 cm) clots of mafic minerals to meter-scale, fine-grained enclaves. Mapping shows that the rapakivi granite forms a sheet-like body that extends across most of the batholith (303 km^2) with a minimum thickness of ~1400 m (Fig. 1B and

1C). Smaller, tabular bodies of leucogranite are common at high elevations within the rapakivi granite and may represent segregations of high-SiO_2 melt (Bachmann and Bergantz, 2004; Lee and Morton, 2015) or intrusion of a different melt composition after the rapakivi granite had mostly crystallized. The normative mineralogy of the rapakivi granite plots along a linear array in the Ab-Or-Qz ternary (Fig. DR1). This array reflects systematic variations in the chemistry of the rapakivi granite that correlate with each sample's vertical position within the sheet. These variations may reflect the vertical stratification expected to develop as silicic magma chambers differentiate (e.g., Lee and Morton, 2015), suggesting that these whole rock analyses do not represent liquid compositions and precluding their use in depth estimates.

Heterogeneous granite: Heterogeneous granite is exposed in the NW part of the batholith (Fig. 1B and 1C) as a 650-m-thick sheet-like body. Internal contacts are present and range from sharp to gradational, implying that the unit is composed of many individual intrusions. However, we could not split the heterogeneous granite into smaller map units due to poor exposure. The rocks are dominantly leucocratic granites and include both perthite-bearing and two-feldspar varieties. A distinctive, ~100-m-thick, fine-grained biotite granite forms the uppermost part of the heterogeneous granites and is found directly underneath the rapakivi granite over a wide area. We project the heterogeneous granite under the granitoid portions of the batholith (303 km^2) for our volume estimate.

Granodiorite: Granodiorite is exposed at low elevations in the extreme NW of the batholith (Fig. 1B). This map unit is composed of heterogeneous granitoids with a higher color index than the heterogeneous granites. The dominant lithology is a medium-grained hornblende granodiorite that includes some rapakivi-textured feldspars.

Quartz Diorite: A small body of hornblende quartz diorite occurs along the SW boundary of the GHB (Fig. 1B). It is medium grained and includes angular xenoliths of the host rock along its outer margin.

Unnamed Subvolcanic Stock: A subvolcanic rhyolitic stock intrudes the rapakivi granite in the NW of the GHB (Fig. 1B). At lower elevations it is a fine-grained, quartz-rich granite and grades into porphyritic rhyolite at higher elevations. The rhyolite is vesiculated and contains quartz phenocrysts, pieces of pumice, and small angular lithic fragments. Its relationship to the GHB is unclear. However, it must postdate the rapakivi granite based on the intrusive contact between the two units.

Al-in-Hornblende Barometry

In order to better assess the emplacement depth of the GHB, we calculated pressures for two samples of the rapakivi granite (NC-MPE-086: 48.57338 -120.63071 and NC-MPE-503: 48.64422 -120.75922) using the Al-in-hornblende barometer. This barometer is based on a linear relationship between the intrusion depth of silicic liquids and the total aluminum content (Al_{tot}) in hornblende. However, the silicic liquid must have been saturated with plagioclase, potassium feldspar, biotite, hornblende, titanite, quartz, magnetite or ilmenite, and a fluid phase during final crystallization for accurate pressure determinations. The

required mineral assemblage was identified in thin section, and the presence of both magnetite and ilmenite was confirmed using energy dispersive spectrometry (Fig. DR2). Hornblende and plagioclase core and rim compositions were measured using a 5 μm spot size on the MIT JEOL-JXA8200 using a 15 kV accelerating voltage and 10 nA beam current. The results are reported in Tables DR1 and DR2. Pressures were calculated using pairs of plagioclase-hornblende cores and plagioclase-hornblende rims using the calibration of Anderson and Smith (1995). Temperatures were estimated using the Blundy and Holland (1990) plagioclase-hornblende thermometer. All temperature and pressure estimates are reported in Table DR3.

The calculated pressures range from 0.05 to 0.30 GPa with an associated uncertainty of 0.06 GPa. Three measurements of hornblende rims give pressures lower than the experimental calibration of the Al-in-hornblende barometer (0.25 GPa: Schmidt, 1992) and hornblende-plagioclase thermometry for these samples gives temperatures below the H_2O-saturated solidus for granitic melts at pressures of <0.5 GPa (Ebadi and Johannes, 1991). Therefore, these results likely do not provide accurate pressure estimates. The remaining measurements give magmatic temperatures and consistent pressures. A mean of these values gives 0.25 ± 0.06 GPa and is at the lower limit of the experimental calibration for the barometer.

Zircon Petrography

Fig. DR3 shows representative cathodeluminescence (CL) images of zircon from GHB granitoids. Imaging was done on the JEOL JXA-733 microprobe at the Massachusetts Institute of Technology using a beam current of 10 nA. Oscillatory zoning is common in the zircons and indicates an igneous origin. No resorbed cores were seen in any of the images, supporting our interpretation that the GHB granitoids were emplaced above zircon saturation temperature. However, petrographic observations demonstrate that zircon is included in, and therefore predated or co-crystallized with, the major rock-forming minerals of the granitoid phases of the GHB (Fig. DR4). We conclude that zircon became saturated shortly after emplacement in the upper crust and that the duration of zircon crystallization approximates the duration of magma crystallization.

U-Pb Zircon Geochronology Methods

Zircons were separated and dated via chemical abrasion-isotope dilution-thermal ionization mass spectrometry (CA-ID-TIMS) following methods slightly modified from Mattinson (2005) and outlined in Appendix A for Eddy et al. (2016). All of the isotopic measurements were made on the VG Sector 54 thermal ionization mass spectrometer (TIMS) at the Massachusetts Institute of Technology and are presented in Table DR4. Pb isotopes were measured by peak hopping on a Daly detector and corrected for fractionation based on repeat analyses of the NBS 981 Pb isotopic standard. U was measured statically on Faraday cups and corrected for fractionation using the known ratio of $^{233}U/^{235}U$ in the EARTHTIME ^{205}Pb-^{233}U-^{235}U isotopic tracer (Condon et al., 2015; McLean et al., 2015). We assume that zircon does not incorporate initial common Pb (Pb_c) during

crystallization and that all measured ^{204}Pb arises from laboratory contamination. We correct for this contamination following the procedures outlined in McLean et al. (2011), using a laboratory Pb_c isotopic composition of $^{206}Pb/^{204}Pb$ = 18.145833 ± 0.475155 (1σ abs.), $^{207}Pb/^{204}Pb$ = 15.303903 ± 0.295535 (1σ abs.), and $^{208}Pb/^{204}Pb$ = 37.107788 ± 0.875051 (1σ abs.), calculated from 149 procedural blanks measured in the MIT isotope geochemistry lab between 2009 and 2015. The mass of Pbc measured in all of these procedural blanks is comparable to the range of Pb_c measured in the analyses presented in this paper and provides strong support for the assumption that no Pb_c is incorporated in zircon during crystallization.

The ^{230}Th isotope is a long-lived ($t^{1/2}$ = 75,400 yr) daughter isotope of ^{238}U, and preferential exclusion of Th during zircon crystallization can lead to initial secular disequilibrium. A correction for the resulting deficiency in radiogenic ^{206}Pb is described by McLean (2011) and Ickert et al. (2015) and is dependent on the $[Th/U]_{zircon}$ and $[Th/U]_{melt}$. The $[Th/U]_{zircon}$ is routinely calculated from zircon measurements using radiogenic ^{208}Pb and assuming concordance between the ^{232}Th-^{208}Pb and U-Pb systems. However, the $[Th/U]_{melt}$ is more difficult to constrain. Two potential methods can be used to derive $[Th/U]_{melt}$, 1) assume a $[Th/U]_{melt}$ using whole rock geochemical measurements or an average value for the rock type being investigated, or 2) use partition coefficients ($f_{ThU}=D_{Th}/D_U$) to calculate $[Th/U]_{melt}$ using $[Th/U]_{zircon}$. We compare both methods in Table DR5. For the approach using constant $[Th/U]_{melt}$, we use $[Th/U]_{melt}=2.8 \pm 1$ (2σ). This value encompasses the range seen in most igneous rocks (Machlus et al., 2015), and is consistent with whole rock measurements from granites within the GHB (Tepper, unpublished data). For the constant partition coefficient approach we use f_{ThU} =0.138 (Stelten et al., 2015) for granitic rocks and f_{ThU} =0.33 (Rubatto and Hermann, 2007) for the marginal tonalite/diorite and apply an arbitrary uncertainty of 1(2σ) on the resulting $[Th/U]_{melt}$.

The difference between data corrected using the two methods is minor and does not affect our interpretations of magma emplacement rates. We prefer the use of a constant f_{ThU} because it seems more reasonable that different $[Th/U]_{zircon}$ within a sample is a result of of changing melt composition either due to local depletion of trace elements around crystallizing trace phases or through changes in bulk melt composition due to fractional crystallization. Nevertheless, trace element partitioning between zircon and melt remains poorly constrained. The value used for granites in this paper (f_{ThU} = 0.138) is an average for coexisting zircon and high-SiO_2 melt erupted from Yellowstone (Stelten et al., 2015). These measurements offer an advantage over other datasets that report partition coefficients for zircon and coexisting high-SiO_2 melt in that it uses trace element measurements from zircon surfaces whose ^{238}U-^{230}Th dates are consistent with crystallization immediately prior to or concurrent with eruption. Other studies either lack corresponding age data or inevitably use a $[Th/U]_{zircon}$ calculated from a mixture of interior and surface domains that may not be in equilibrium with the matrix glass. In Fig. DR5 we show that the Stelten et al. (2015) value reproduces the range of whole rock Th/U measurements for GHB granites for the typical range of $[Th/U]_{zircon}$ values from our dataset.

Data reduction was done using the U-Pb_Redux software package (Bowring et al., 2011) and used the decay constants for ^{235}U and ^{238}U presented in Jaffey et al. (1971). All isotopic ratios are presented in Table DR4 and shown as concordia plots in Fig. DR6.

Magma Emplacement Rates

Magma emplacement rates were estimated for the GHB using our volume estimates (with no assigned uncertainty) and durations (Δt) calculated using Monte Carlo simulations with 10^7 iterations. The simulations found the difference between randomly selected dates from normal distributions with a mean value and 2σ variability equal to the weighted mean dates and 2σ uncertainty of our oldest and youngest sample within each unit. In cases where the oldest and youngest samples substantially overlap within uncertainty, we used the absolute value of the calculated difference to prevent negative durations. The distribution of results is shown in Fig. 2B. Fig. DR7 compares these results with magma emplacement rates, recalculated using the same technique, from previously published geochronologic data from upper-crustal granitoid plutonic complexes (Table DR6). As noted in the text, the rapakivi granite represents the highest magma emplacement rates documented in a granitoid plutonic complex.

References

Anderson, J.L. and Smith, D.R., 1995, The effects of temperature and fo_2 on the Al-in-hornblende barometer: American Mineralogist, v. 80, p. 549-559, doi: 10.2138/am-1995-5-615.

Annen, C., 2009, From plutons to magma chambers: thermal constraints on the accumulation of eruptible silicic magma in the upper crust: Earth and Planetary Science Letters, v. 284, p. 409-416, doi: 10.1016/j.epsl.2009.05.006.

Bachmann, O., and Bergantz, G.W., 2004, On the origin of crystal-poor rhyolites: extracted from batholithic crystal mushes: Journal of Petrology, v. 45, p. 1565-1582, doi: 10.1093/petrology/egh019.

Blundy, J., and Cashman, K., 2001, Ascent-driven crystallization of dacite magmas at Mount St Helens, 1980-1986: Contributions to Mineralogy and Petrology, v. 140, p. 631-650, doi: 10.1007/s004100000219.

Blundy, J., and Holland, T.J.B., 1990, Calcic amphibole equilibria and a new amphibole-plagioclase geothermometer: Contributions to Mineralogy and Petrology, v. 104, p. 208-224, doi: 10.1007/BF00306444.

Bowring, J.F., McLean, N.M., and Bowring, S.A., 2011, Engineering cyber infrastructure for U-Pb geochronology: Tripoli and U-Pb_Redux: Geochemistry, Geophysics, and Geosystems, v. 12, doi: 10.1029/2010GC003479.

Boggs, R.C., 1984, Mineralogy and geochemistry of the Golden Horn batholith, northern Cascades, Washington [PhD Thesis]: Santa Barbara, University of California, 187 p.

Coleman, D.S., Gray, W., and Glazner, A.F., Rethinking the emplacement and evolution of zoned plutons: geochronologic evidence for incremental assembly of the Tuolumne Intrusive Suite, California: Geological Society of America Bulletin, v. 32, p. 433-436, doi: 10.1130/G20220.1.

Condon, D.J., Schoene, B., McLean, N.M., Bowring, S.A., and Parrish, R.R., 2015, Metrology and traceability of U-Pb isotopic dilution geochronology (EARTHTIME tracer calibration part I): Geochimica et Cosmochimica, v. 164, p 464-480, doi: 10.1016/j.gca.2015.05.026.

Davis, J.W., Coleman, D.S., Gracely, J.T., Gaschnig, R., and Stearns, M., 2012, Magma accumulation rates and thermal histories of plutons of the Sierra Nevada batholith, CA: Contributions to Mineralogy and Petrology, v., 163, p. 449-465, doi: 10.1007/s00410-011-0683-7.

Eddy, M.P., Bowring, S.A., Umhoefer, P.J., Miller, R.B., McLean, N.M., and Donaghy, E.E., 2016, High resolution temporal and stratigraphic record of Siletzia's accretion and triple junction migration from nonmarine sedimentary basins in central and western Washington: Geological Society of America Bulletin, doi: 10.1130/B31335.1.

Ebadi, A., and Johannes, W., 1991, Beginning of melting and composition of first melts in the system Qz-Ab-Or-H2O-CO2: Contributions to Mineralogy and Petrology, v. 106, p. 286-295, doi: 10.1007/BF00324558.

Frazer, R.E., Coleman, D.S., and Mills, R.D., 2014, Zircon U-Pb geochronology of the Mount Givens Granodiorite: Implications for the genesis of large volumes of eruptible magma: Journal of Geophysical Research Solid Earth, v. 119, p. 2907-2924, doi: 10.1002/2013JB010716.

Gelman, S.E., Gutierrez, F.J., and Bachmann, O., 2013, On the longevity of large upper crustal silicic magma reservoirs: Geology, v. 41, p. 759-762, doi: 10.1130/G34241.1.

Ickert, R.B., Mundil, R., Magee Jr., C.W., and Mulcahy, S.R., 2015, The U-Th-Pb systematics of zircon from the Bishop Tuff: A case study in challenges to high-precision Pb/U geochronology at the millennial scale: Geochimica et Cosmochimica Acta, v. 168, p. 88-110, doi: 10.1016/j.gca.2015.07.018.

Jaffey, A.H., Flynn, K.F., Glendenin, L.E., Bentley, W.C., Essling, A.M., 1971, Precision measurement of half-lives and specific activities of 235U and 38U: Physical Review C, v. 4, p. 1889-1906, doi: 10.1103/PhysRevC.4.1889.

John, B.E., and Blundy, J.D., 1993, Emplacement-related deformation of granitoid magmas, southern Adamello Massif, Italy: Geological Society of America Bulletin, v. 105, p. 1517-1541, doi: 10.1130/0016-7606(1993)105<1517:ERDOGM>2.3.CO;2.

Lee, C.A., and Morton, D.M., 2015, High silica granites: terminal porosity and crystal settling in shallow magma chambers: Earth and Planetary Science Letters, v. 409, p. 23-31, doi: 10.1016/j.epsl.2014.10.040.

Leuthold, J., Muntener, O., Baumgartner, L.P., Putlitz, B., Ovtcharova, M., and Schaltegger, U., 2012, Tim resolved construction of a bimodal laccolith (Torres del Paine, Patagonia): Earth and Planetary Science Letters, v. 325-326, p. 85-92, doi: 10.1016/j.epsl.2012.01.032.

Machlus, M.L., Ramezani, J., Bowring, S.A., Hemming, S.R., Tsukui, K., and Clyde, W.C., 2015, A strategy for cross-calibrating U-Pb chronology and astrochronology of sedimentary sequences: an example from the Green River Formation, Wyoming, USA: Earth and Planetary Sciences, v. 413, p. 70-78, doi:10.1016/j.epsl.2014.12.009.

Mattinson, J.M., 2005, Zircon U-Pb chemical abrasion ("CA-TIMS") method: Combined annealing and multi-step partial dissolution analysis for improved precision and accuracy of zircon ages: Chemical Geology, v. 220, p. 47-66, doi: 10.1016/j.chemgeo.2005.03.011.

Matzel, J.E.P., Bowring, S.A., and Miller, R.B., 2006, Time scales of pluton construction at differeing crustal levels: Examples from the Mount Stuart and Tenpeak intrusions, North Cascades, Washington: Geological Society of America Bulletin, v. 118, p. 1412-1430, doi: 10.1130/B25923.1.

McLean, N.M., Bowring, J.F., and Bowring, S.A., 2011, An algorithm for U-Pb isotope dilution data reduction and uncertainty propagation: Geochemistry, Geophysics, Geosystems, v. 12, Q0AA19, doi: 10.1029/2010GC003478.

McLean, N.M., Condon, D.J., Condon, B., and Bowring, S.A., 2015, Evaluating uncertainties in the calibration of isotopic reference materials and multi-element isotopic tracers (EARTHTIME tracer calibration II): Geochimica et Cosmochimica, v. 164, p. 481-501, doi: 10.1016/j.gca.2015.02.040.

McNulty, B.A., Tobish, O.T., Cruden, A.R., and Giler, S., 2000, Multistage emplacement of the Mount Givens pluton, central Sierra Nevada batholith, California: Geological Society of America Bulletin, v. 112, p. 119-135, doi: 10.1130/0016-7606(2000)112<119:MEOTMG>2.0.CO;2.

Memeti, V., Paterson, S., Matzel, J., Mundil, R., and Okaya, D., 2010, Magmatic lobes as "snapshots" of magma chamber growth and evolution in large, composite batholiths: An example from the Tuolumne intrusion, Sierra Nevada, California: Geological Society of America Bulletin, v. 122, p. 1912-1931, doi: 10.1130/B30004.1.

Mills, R.D., and Coleman, D.S., 2013, Temporal and chemical connections between plutons and ignimbrites from the Mount Princeton magmatic center: Contributions to Mineralogy and Petrology, v. 165, p. 961-980, doi: 10.1007/s00410-012-0843-4.

Misch, P., 1965, Alkaline granite amidst the calc-alkaline intrusive suite of the Northern Cascades, Washington: Geological Society of America Special Papers, v. 87, p. 216-217.

Rubatto, D., and Hermann, J., 2007, Experimental zircon/melt and zircon/garnet trace element partitioning and implications for the geochronology of crustal rocks: Chemical Geology, v. 241, p. 38-61, doi: 10.1016/j.chemgeo.2007.01.027.

Schmidt, M.W., 1992, Amphibole composition in tonalite as a function of pressure: an experimental calibration of the Al-in-hornblende barometer: Contributions to Mineralogy and Petrology, v. 110, p. 304-310, doi: 10.1007/BF00310745.

Schoene, B., Schaltegger, U., Brack, P., Latkoczy, C., Stracke, A., and Gunther, D., Rates of magma differentiation and emplacement in a ballooning pluton recorded by U-Pb TIMS-TEA, Adamello batholith, Italy: Earth and Planetary Science Letters, v. 355-356, p. 162-173, doi: 10.1016/j.epsl.2012.08.019.

Stelten, M.E., Cooper, K.M., Vazquez, J.A., Calvert, A.T., and Glessner, J.J.G., 2015, Mechanisms and timescales of generating eruptible rhyolitic magmas at Yellowstone caldera from zircon and sanidine geochronology and geochemistry: Journal of Petrology, v. 56, p. 1607-1642, doi: 10.1093/petrology/egv047.

Stull, R.J., 1969, The geochemistry of the southeastern portion of the Golden Horn batholith, Northern Cascades, Washington [Ph.D. thesis]: Seattle, University of Washington, 127 p.

Stull, R.J., 1978, Mantled feldspars from the Golden Horn batholith, Washington: Lithos, v. 11, p. 243-249, doi: 10.1016/0024-4937(78)90024-5.

Tappa, M.J., Coleman, D.S., Mills, R.D., and Samperton, K.M., 2011, The plutonic record of a silicic ignimbrite from the Latir volcanic field, New Mexico: Geochemistry, Geophysics, Geosystems, v. 12, Q10011, doi: 10.1029/2011GC003700.

Figure Captions

Figure DR1: Plot showing the H_2O-saturated eutectic in the quartz (Qz), albite (Ab), orthoclase (Or) system for pressures ranging from 1 to 0.1 GPa (Ebadi and Johannes, 1991). The normative mineralogy for geochemical analyses by Stull (1969) of the peralkaline, hypersolvus, and rapakivi granites are shown and projected using the method of Blundy and Cashman (2001). Compositions for the peralkaline and hypersolvus granites cluster around the 0.2 GPa H_2O-saturated eutectic.

Figure DR2: Back scattered electron (BSE) image of an amphibole in sample NC-MPE-503 from the rapakivi granite of the GHB. The image shows the required assemblage for Al-in-hornblende barometry.

Figure DR3*:* Representative CL images of zircon from granites within the GHB. Oscillatory zoning is clearly seen, indicating an igneous origin. No resorbed cores were seen in any of the images, supporting the inference that GHB magmas intruded above their zircon saturation temperatures.

Figure DR4: Select photomicrographs showing zircon included in major, rock-forming minerals in the granodiorite (NC-MPE-200), hypersolvus granite (NC-MPE-378A), rapakivi granite (NC-MPE-086), and heterogeneous granite (NC-MPE-485). The photomicrograph for NC-MPE-200 is in plane polarized light, while the others are all in cross-polarized light.

Figure DR5: Plot showing the relationship between f_{ThU} and the calculated $[Th/U]_{melt}$ for different $[Th/U]_{zircon}$. The Stelten et al. (2015) value of f_{ThU}=0.138 reproduces the range of whole rock [Th/U] values seen in GHB rocks (Tepper, unpublished data) for the range of $[Th/U]_{zircon}$ seen in our analyses (Table DR4).

Figure DR6: Traditional concordia plots for all of the dated samples presented in this study. All $^{206}Pb/^{238}U$ ratios are Th-corrected. Dates used in weighted mean calculations are shown as red ellipses, those excluded are shown in gray.

Figure DR7: Plot showing volumes and magma emplacement rates for upper crustal granitoid plutons modified from Mills and Coleman (2013) and Frazer et al. (2014). The shaded field represents the rates needed in thermal models to build a large-volume, high-SiO_2 magma chamber (Annen, 2009; Gelman et al., 2013). All emplacement rates represent the mode of Monte Carlo simulations and uncertainties represent the 95% confidence interval. Labels correspond to the numbered intrusive complexes in Table DR6. Volume estimates are limited to the exposed volume (volume = area x topographic relief) to facilitate comparison to the GHB data.

TABLE DR1: ELECTRON MICROPROBE ANALYSES OF HORNBLENDE

Sample Name	SiO_2	TiO_2	K_2O	MnO	Na_2O	Cr_2O_3	Al_2O_3	CaO	FeO_{tot}	MgO	Total*
NC-MPE-503 H1 Core	46.89	1.40	0.64	0.61	1.97	0.01	6.29	10.41	19.80	10.80	98.83
NC-MPE-503 H1 Rim	49.08	0.63	0.47	0.85	1.47	0.00	4.09	10.61	20.68	11.19	99.07
NC-MPE-503 H2 Core	45.75	1.68	0.68	0.52	2.09	0.00	6.85	10.63	21.43	9.26	98.89
NC-MPE-503 H2 Rim	48.68	0.75	0.56	0.83	1.43	0.00	4.75	10.88	20.30	10.59	98.78
NC-MPE-503 H3 Core	44.14	1.59	0.81	0.83	2.23	0.02	7.95	10.59	22.01	9.14	99.32
NC-MPE-503 H3 Rim	46.01	1.58	0.67	0.49	2.18	0.00	6.70	10.45	19.59	10.99	98.65
NC-MPE-503 H4 Core	45.87	1.78	0.67	0.58	2.05	0.00	6.76	10.56	20.74	10.17	99.18
NC-MPE-503 H4 Rim	47.68	0.90	0.63	0.86	1.71	0.00	5.08	10.76	20.75	10.59	98.96
NC-MPE-086 H1 Core	45.87	1.73	0.73	0.68	2.19	0.00	6.82	10.41	20.86	10.16	99.45
NC-MPE-086 H1 Rim	46.21	1.45	0.72	0.64	1.91	0.02	6.77	10.66	20.17	10.46	99.01
NC-MPE-086 H2 Core	47.32	1.10	0.66	0.80	1.86	0.00	5.56	10.62	20.60	10.74	99.26
NC-MPE-086 H2 Rim	46.16	1.35	0.76	0.77	1.88	0.03	6.58	10.59	20.98	9.76	98.86

* All analyses are reported in wt %.

TABLE DR2: ELECTRON MICROPROBE ANALYSES OF PLAGIOCLASE

Sample	SiO_2	CaO	FeO	Na_2O	Al_2O_3	K_2O	Total*
NC-MPE-503 P1 Core	65.91	2.29	0.06	10.50	21.41	0.34	100.52
NC-MPE-503 P1 Rim	67.89	0.59	0.19	11.72	19.85	0.09	100.33
NC-MPE-503 P2 Core	64.44	3.62	0.15	10.01	22.53	0.50	101.25
NC-MPE-503 P2 Rim	65.06	3.06	0.16	9.98	21.89	0.77	100.92
NC-MPE-503 P3 Core	64.19	3.96	0.18	9.32	22.63	0.49	100.77
NC-MPE-503 P3 Rim	66.68	1.76	0.12	10.49	20.89	0.53	100.47
NC-MPE-503 P4 Core	64.80	3.51	0.16	9.88	22.45	0.41	101.22
NC-MPE-503 P4 Rim	68.66	0.97	0.13	11.31	19.88	0.22	101.17
NC-MPE-086 P1 Core	65.72	2.57	0.11	9.98	21.53	0.88	100.79
NC-MPE-086 P1 Rim	66.46	2.06	0.26	10.40	20.89	0.63	100.70
NC-MPE-086 P2 Core	63.87	3.65	0.19	9.10	22.54	0.74	100.08
NC-MPE-086 P2 Rim	66.07	2.40	0.11	10.21	21.25	0.75	100.79

* All measurements are reported in wt %.

TABLE DR3: THERMOBAROMETRY RESULTS

Sample	Al-in-Hornblende Pressure* (GPa)	Plagioclase-Hornblende Temperature† (°C)
NC-MPE-503 H1-P1 Core	0.23	669.4
NC-MPE-503 H1-P1 Rim	0.05	613.5
NC-MPE-503 H2-P2 Core	0.27	686.3
NC-MPE-503 H2-P2 Rim	0.11	630.1
NC-MPE-503 H3-P3 Core	0.30	735.2
NC-MPE-503 H3-P3 Rim	0.26	677.8
NC-MPE-503 H4-P4 Core	0.25	691.6
NC-MPE-503 H4-P4 Rim	0.14	630.5
NC-MPE-086 H1-P1 Core	0.26	690.9
NC-MPE-086 H1-P1 Rim	0.26	676.9
NC-MPE-086 H1-P1 Core	0.17	672.1
NC-MPE-086 H1-P1 Rim	0.25	675.1

* All pressures were calculated using the calibration of Anderson and Smith (1995).
† Temperatures were calculated using Blundy and Holland (1990).

TABLE DR4: CA-ID-TIMS U-Pb ZIRCON GEOCHRONOLOGY RESULTS

Frac.	Dates $^{206}Pb/^{238}U^{*}$	2σ abs.	$^{207}Pb/^{235}U^{\dagger}$	2σ abs.	$^{207}Pb/^{206}Pb^{\dagger}$	2σ abs.	% Disc.[§]	Corr. Coef.	Composition Th/U[#]	Pb_{c} (pg)[*]	Pb*/Pb_{c}[††]	Isotopic Ratios $^{206}Pb/^{204}Pb$[§§]	$^{208}Pb/^{206}Pb$[##]	$^{206}Pb/^{238}U^{*,\#\#}$	2σ %	$^{207}Pb/^{235}U^{\#\#}$	2σ %	$^{207}Pb/^{206}Pb^{*,\#\#}$	2σ %
NC-MPE-438 (48.50682 -120.66447[***])																			
z1	48.467	0.063	48.55	0.42	56	21	14.09	0.275	0.25	0.62	25	1601	0.081	0.0075355	0.086	0.04898	0.88	0.04716	0.86
z2	48.567	0.087	48.96	0.85	72	41	32.64	0.362	0.29	1.98	12	743	0.094	0.007551	0.16	0.04940	1.8	0.04747	1.7
z3	48.472	0.071	48.39	0.62	48	30	-1.38	0.429	0.29	0.48	17	1101	0.092	0.0075361	0.12	0.04881	1.3	0.04699	1.3
z5	48.479	0.092	49.08	0.95	82	46	41.11	0.365	0.32	2.94	10	667	0.104	0.007537	0.18	0.04953	2.0	0.04768	1.9
z6	48.432	0.049	48.41	0.17	51.1	8.1	5.31	0.378	0.31	0.38	69	4374	0.098	0.0075298	0.066	0.04883	0.36	0.04706	0.34
NC-MPE-511 (48.50197 -120.62159[***])																			
z1	48.362	0.033	48.403	0.072	55.1	2.9	12.32	0.625	0.45	0.37	189	11430	0.146	0.0075158	0.067	0.048824	0.15	0.047136	0.12
z3	48.347	0.046	48.57	0.44	64	22	25.11	0.319	0.42	5.20	22	1377	0.135	0.0075134	0.096	0.04900	0.94	0.04732	0.91
z4	48.325	0.033	48.39	0.13	56.1	5.8	13.98	0.456	0.37	0.51	97	5971	0.119	0.0075100	0.067	0.04881	0.27	0.04716	0.24
z5	48.328	0.058	48.35	0.10	54.2	3.9	10.97	0.625	0.40	0.46	193	11798	0.129	0.0075104	0.12	0.04877	0.21	0.047119	0.16
z6	48.357	0.032	48.44	0.13	57.3	6.1	15.73	0.533	0.42	0.41	91	5568	0.136	0.0075151	0.065	0.04886	0.28	0.04718	0.25
z7	48.345	0.034	48.266	0.096	49.0	4.1	1.52	0.570	0.42	0.55	142	8656	0.135	0.0075131	0.071	0.048683	0.20	0.047017	0.17
NC-MPE-093 (48.52964 -120.64862[***])																			
z1	48.247	0.030	48.35	0.19	58.0	9.0	16.98	0.371	0.37	0.75	54	3377	0.118	0.0074978	0.063	0.04877	0.40	0.04719	0.38
z2	48.321	0.073	48.61	0.86	67	42	28.30	0.353	0.41	0.73	12	730	0.132	0.007509	0.15	0.04903	1.8	0.04738	1.8
z6	48.297	0.031	48.36	0.25	56	12	14.11	0.340	0.38	0.35	42	2620	0.123	0.0075056	0.064	0.04878	0.53	0.04716	0.51
z7	48.288	0.054	48.49	0.59	63	29	23.83	0.414	0.39	0.33	18	1099	0.125	0.0075042	0.11	0.04892	1.2	0.04730	1.2
z9	48.24	0.14	48.9	1.7	84	84	42.85	0.329	0.44	1.69	6	368	0.140	0.007496	0.29	0.0493	3.6	0.0477	3.6
z12	48.315	0.050	48.53	0.47	64	23	24.44	0.319	0.39	1.39	21	1300	0.125	0.0075084	0.10	0.04896	1.0	0.04731	0.97
NC-MPE-378A (48.57325 -120.84033[***])																			
z16	48.235	0.062	48.54	0.70	68	34	29.43	0.350	0.38	1.17	14	881	0.123	0.0074960	0.13	0.04897	1.5	0.04740	1.4
z25	48.210	0.038	48.23	0.25	54	12	10.36	0.438	0.39	0.34	46	2830	0.125	0.0074920	0.079	0.04864	0.53	0.04711	0.49
z26	48.228	0.044	48.15	0.35	49	17	1.80	0.247	0.36	0.50	29	1831	0.115	0.0074948	0.091	0.04857	0.74	0.04702	0.72
z27	48.207	0.049	48.18	0.55	51	27	6.50	0.336	0.51	0.69	19	1132	0.162	0.0074915	0.10	0.04859	1.2	0.04707	1.1
z28	48.251	0.055	48.43	0.56	62	27	22.34	0.370	0.94	0.44	23	1241	0.300	0.0074984	0.11	0.04885	1.2	0.04727	1.1
z16	48.235	0.062	48.54	0.70	68	34	29.43	0.350	0.38	1.17	14	881	0.123	0.0074960	0.13	0.04897	1.5	0.04740	1.4
NC-MPE-088 (48.54091 -120.63500[***])																			
z1	48.169	0.065	48.24	0.36	56	17	14.48	0.340	0.40	0.33	30	1840	0.127	0.007486	0.14	0.04865	0.76	0.04716	0.73
z2	48.199	0.042	48.71	0.43	79	21	38.79	0.400	0.38	0.36	24	1523	0.121	0.0074903	0.088	0.04914	0.90	0.04760	0.86
z3	48.205	0.035	48.29	0.30	57	14	15.51	0.393	0.38	0.36	36	2255	0.120	0.0074912	0.072	0.04870	0.63	0.04717	0.60
z4	48.224	0.046	48.50	0.45	67	22	28.12	0.297	0.37	0.23	25	1542	0.120	0.0074942	0.096	0.04893	0.95	0.04737	0.93
z5	48.207	0.053	48.42	0.58	63	28	24.11	0.387	0.37	0.30	18	1109	0.119	0.0074915	0.11	0.04884	1.2	0.04730	1.2
z6	48.223	0.099	48.4	1.3	61	65	21.36	0.289	0.37	0.44	8	496	0.119	0.007494	0.21	0.0488	2.8	0.0473	2.7
NC-MPE-583 (48.55848 -120.69115[***])																			
z1	48.196	0.033	48.39	0.16	62.7	7.2	23.29	0.512	0.38	0.48	78	4818	0.123	0.0074898	0.068	0.04881	0.33	0.04729	0.30
z2	48.164	0.033	48.24	0.21	56	10	14.87	0.379	0.44	0.50	53	3223	0.141	0.0074848	0.067	0.04865	0.45	0.04716	0.43
z3	48.158	0.059	48.43	0.62	66	30	27.67	0.355	0.38	0.74	17	1051	0.121	0.0074838	0.12	0.04885	1.3	0.04736	1.3
z4	48.212	0.057	48.26	0.63	55	31	13.21	0.373	0.41	0.53	16	1005	0.131	0.0074923	0.12	0.04868	1.3	0.04714	1.3
z5	48.256	0.090	48.9	1.1	85	53	43.41	0.343	0.44	1.10	9	583	0.141	0.007499	0.19	0.0493	2.3	0.0477	2.2
z6	48.187	0.030	48.50	0.23	69	11	29.85	0.340	0.39	0.29	47	2931	0.123	0.0074883	0.061	0.04892	0.48	0.04740	0.46
NC-MPE-450 (48.65726 -120.81995[***])																			
z4	48.194	0.074	48.63	0.77	75	37	35.55	0.390	0.37	0.41	14	857	0.118	0.007489	0.15	0.04905	1.6	0.04753	1.6
z5	48.105	0.092	47.8	1.1	36	54	-32.63	0.402	0.39	0.30	10	621	0.126	0.007476	0.19	0.0482	2.3	0.0468	2.2
z6	48.144	0.030	48.30	0.20	60.7	9.8	20.85	0.328	0.35	0.57	51	3195	0.111	0.0074817	0.061	0.04872	0.43	0.04725	0.41
z7	48.119	0.047	48.03	0.51	48	25	0.40	0.390	0.38	0.55	20	1248	0.122	0.0074778	0.098	0.04844	1.1	0.04700	1.1

z8	48.135	0.042	48.43	0.39	68	19	29.17	0.454	0.34	0.42	28	1746	0.108	0.0074803	0.088	0.04886	0.83	0.04739	0.79
z9	48.168	0.039	48.40	0.35	64	17	25.26	0.366	0.36	0.59	29	1806	0.114	0.0074855	0.080	0.04882	0.74	0.04732	0.71
NC-MPE-523 (48.54485 -120.68233***)																			
z2	48.132	0.036	47.99	0.27	46	13	-4.86	0.312	0.34	0.29	44	2724	0.110	0.0074798	0.074	0.04840	0.57	0.04695	0.55
z3	48.129	0.027	48.05	0.14	48.7	6.6	1.28	0.354	0.35	0.34	90	5588	0.113	0.0074794	0.055	0.04846	0.29	0.04701	0.27
z4	48.176	0.035	48.36	0.23	62	11	22.47	0.446	0.34	0.58	48	2981	0.108	0.0074867	0.072	0.04878	0.49	0.04727	0.46
z5	48.185	0.076	48.47	0.74	67	36	28.49	0.416	0.38	1.33	14	906	0.122	0.007488	0.16	0.04889	1.6	0.04738	1.5
z7	48.15	0.10	48.2	1.4	57	71	16.23	0.353	0.33	0.62	8	526	0.105	0.007482	0.21	0.0487	3.1	0.0472	3.0
z8	48.120	0.078	47.65	0.86	29	43	-66.98	0.423	0.39	0.92	13	799	0.124	0.007478	0.16	0.04805	1.8	0.04662	1.8
NC-MPE-086 (48.57338 -120.63071***)																			
z1	48.128	0.029	48.32	0.19	62.6	9.3	23.25	0.230	0.41	0.27	56	3459	0.131	0.0074792	0.059	0.04874	0.40	0.04729	0.39
z2	48.156	0.030	48.23	0.18	56.7	8.9	15.19	0.329	0.56	0.39	63	3706	0.180	0.0074835	0.062	0.04865	0.39	0.04717	0.37
z3	48.098	0.041	48.26	0.29	61	14	21.24	0.363	0.41	0.35	39	2419	0.132	0.0074744	0.085	0.04868	0.62	0.04725	0.60
z4	48.151	0.028	48.28	0.18	59.5	8.6	19.18	0.405	0.40	0.33	67	4091	0.127	0.0074828	0.057	0.04870	0.38	0.04722	0.36
z5	48.134	0.046	48.29	0.17	60.9	7.9	21.08	0.373	0.39	0.41	70	4277	0.126	0.0074801	0.096	0.04871	0.36	0.04725	0.33
z6	48.159	0.058	48.24	0.29	57	15	15.87	0.147	0.74	0.85	39	2197	0.236	0.0074841	0.12	0.04866	0.62	0.04718	0.62
NC-MPE-510 (48.62438 -120.76897***)																			
z1	48.130	0.032	48.15	0.24	54	12	10.77	0.435	0.39	0.34	49	3007	0.126	0.0074795	0.066	0.04856	0.51	0.04711	0.48
z2	48.126	0.045	47.92	0.41	42	20	-13.07	0.343	0.40	0.44	27	1691	0.128	0.0074788	0.094	0.04833	0.87	0.04689	0.84
z3	48.093	0.056	47.84	0.62	40	31	-21.08	0.361	0.33	0.49	16	1021	0.105	0.0074738	0.12	0.04824	1.3	0.04683	1.3
z4	48.152	0.029	48.12	0.21	51	10	6.04	0.273	0.39	0.48	49	3054	0.123	0.0074830	0.059	0.04853	0.44	0.04706	0.42
z5	48.155	0.076	48.58	0.92	74	45	35.42	0.327	0.35	2.63	10	663	0.112	0.007483	0.16	0.04901	1.9	0.04752	1.9
z6	48.109	0.032	48.29	0.26	62	12	22.73	0.404	0.40	0.56	43	2657	0.127	0.0074762	0.067	0.04871	0.54	0.04728	0.52
NC-MPE-499 (48.57868 -120.83591***)																			
z1	48.144	0.080	47.84	0.47	37	23	-28.15	0.310	0.36	0.76	31	1943	0.114	0.007482	0.17	0.04825	1.0	0.04679	0.96
z2	48.148	0.089	48.29	0.22	60	10	19.71	0.431	0.35	0.43	56	3476	0.111	0.007482	0.19	0.04870	0.47	0.04723	0.42
z3	48.119	0.030	48.20	0.19	56.9	9.2	15.64	0.404	0.33	0.51	56	3534	0.106	0.0074778	0.062	0.04862	0.41	0.04717	0.38
z4	48.101	0.033	48.16	0.18	55.5	8.6	13.53	0.349	0.36	0.45	60	3742	0.114	0.0074750	0.069	0.04857	0.38	0.04715	0.36
z5	48.132	0.036	48.19	0.33	56	16	14.17	0.345	0.36	0.44	35	2182	0.115	0.0074798	0.074	0.04861	0.70	0.04715	0.68
z6	48.124	0.045	48.27	0.28	60	14	20.52	0.295	0.39	0.87	38	2347	0.124	0.0074785	0.094	0.04869	0.59	0.04724	0.57
NC-MPE-200 (48.65371 -120.85905***)																			
z1	47.987	0.088	48.3	1.1	67	53	29.02	0.358	0.45	0.58	9	591	0.144	0.007457	0.18	0.0487	2.3	0.0474	2.2
z20	48.004	0.073	47.74	0.87	39	44	-21.89	0.343	0.53	1.14	12	712	0.169	0.007460	0.15	0.04814	1.9	0.04683	1.8
z25	48.080	0.073	48.30	0.87	64	43	25.04	0.342	0.48	1.28	12	716	0.153	0.007472	0.15	0.04872	1.8	0.04731	1.8
z32	48.078	0.059	47.92	0.49	45	24	-7.72	0.512	0.50	0.47	22	1335	0.161	0.0074715	0.12	0.04832	1.1	0.04693	0.99
z33	48.03	0.11	48.8	1.4	90	70	46.82	0.341	0.53	1.84	7	435	0.168	0.007464	0.24	0.0492	3.0	0.0478	2.9
NC-MPE-565A (48.63493 -120.84813***)																			
z1	47.808	0.029	47.83	0.21	53	10	10.57	0.336	0.44	0.31	59	3594	0.140	0.0074292	0.060	0.04823	0.44	0.04710	0.43
z2	47.792	0.046	47.87	0.32	56	16	15.19	0.375	0.54	0.70	34	2047	0.174	0.0074267	0.097	0.04827	0.69	0.04716	0.65
z3	47.732	0.073	47.82	0.43	57	21	16.38	0.375	0.41	0.80	25	1529	0.130	0.007417	0.15	0.04822	0.92	0.04717	0.88
z4	47.820	0.038	47.74	0.38	49	19	1.84	0.332	0.52	0.45	28	1649	0.167	0.0074311	0.080	0.04814	0.81	0.04701	0.79
z5	47.785	0.040	47.75	0.33	50	16	5.50	0.398	0.46	0.25	38	2284	0.146	0.0074255	0.083	0.04815	0.70	0.04705	0.67
NC-MPE-485 (48.66853 -120.90965***)																			
z1	47.73	0.11	47.5	1.3	43	67	-9.99	0.358	0.44	0.54	8	477	0.141	0.007416	0.23	0.0479	2.9	0.0469	2.8
z2	47.743	0.026	47.78	0.11	54.2	5.1	12.11	0.360	0.48	0.39	122	7312	0.155	0.0074191	0.053	0.04818	0.23	0.047119	0.21
z3	47.698	0.059	47.74	0.62	55	31	12.92	0.450	0.44	0.47	16	1000	0.141	0.0074120	0.12	0.04814	1.3	0.04713	1.3
z4	47.725	0.029	47.71	0.14	51.8	6.5	8.07	0.655	0.40	0.21	109	6721	0.127	0.0074162	0.061	0.04811	0.31	0.04707	0.27
z5	47.723	0.028	47.69	0.18	50.7	8.6	6.11	0.354	0.39	0.25	66	4096	0.124	0.0074159	0.058	0.04809	0.38	0.04705	0.36
z6	47.952	0.045	48.04	0.48	57	23	16.07	0.409	0.44	0.35	22	1361	0.140	0.0074517	0.094	0.04845	1.0	0.04718	0.98
NC-MPE-517 (48.63261 -120.80870***)																			

z1	48.344	0.044	48.58	0.46	65	23	25.56	0.340	0.39	1.03	21	1322	0.126	0.0075129	0.092	0.04901	0.98	0.04733	0.95
z2	48.603	0.062	48.33	0.65	39	32	-23.59	0.404	0.25	0.32	15	993	0.079	0.0075533	0.13	0.04874	1.4	0.04683	1.3
z4	48.266	0.054	48.40	0.48	60	23	19.05	0.384	0.44	0.40	24	1498	0.141	0.0075008	0.11	0.04882	1.0	0.04722	0.97
z5	47.988	0.052	48.30	0.49	68	24	30.00	0.380	0.79	0.66	25	1411	0.252	0.0074573	0.11	0.04872	1.0	0.04740	1.0
z6	48.198	0.033	48.33	0.27	59	13	19.04	0.360	0.42	0.47	39	2421	0.133	0.0074901	0.069	0.04875	0.57	0.04722	0.55
z7	48.13	0.19	48.5	2.4	73	120	34.31	0.364	0.93	0.69	5	274	0.297	0.007480	0.39	0.0490	5.1	0.0475	4.9
z8	48.192	0.030	48.07	0.13	46.8	5.9	-2.73	0.447	0.51	0.47	117	6941	0.164	0.0074891	0.062	0.04848	0.27	0.04697	0.24

* Corrected for initial Th/U disequilibrium using radiogenic ^{208}Pb and f_{ThU}=0.138 for granitoids (Stelten et al., 2015) or f_{ThU}=0.33 for the diorite (Rubatto and Hermann, 2007).
† Isotopic dates calculated using the decay constants λ238 = 1.55125E-10 and λ235 = 9.8485E-10 (Jaffey et al. 1971).
§ % discordance = 100 - (100 * ($^{206}Pb/^{238}U$ date) / ($^{207}Pb/^{206}Pb$ date))
# Th contents calculated from radiogenic ^{208}Pb and the $^{207}Pb/^{206}Pb$ date of the sample, assuming concordance between U-Th and Pb systems.
** Total mass of common Pb.
†† Ratio of radiogenic Pb (including ^{208}Pb) to common Pb.
§§ Measured ratio corrected for fractionation and spike contribution only.
Measured ratios corrected for fractionation, tracer and blank.
*** All locations reported using WGS 84.

TABLE DR5: COMPARISON OF DIFFERENT Th-CORRECTION METHODS

Sample	Weighted Mean $^{206}Pb/^{238}U$ Date (Ma) Constant f_{ThU}* Correction	Weighted Mean $^{206}Pb/^{238}U$ Date (Ma) Constant $[Th/U]_{Magma}$† Correction	Difference Between Methods (Ma)
NC-MPE-438	48.468 ± 0.030/0.037/0.064 (MSWD=1.84)	48.485 ± 0.022/0.031/0.060 (MSWD=2.87)	0.017
NC-MPE-511	48.346 ± 0.015/0.026/0.058 (MSWD=0.69)	48.345 ± 0.015/0.026/0.058 (MSWD=0.60)	0.001
NC-MPE-093	48.281 ± 0.018/0.028/0.059 (MSWD=1.91)	48.281 ± 0.018/0.028/0.059 (MSWD=1.88)	0.000
NC-MPE-378A	48.223 ± 0.021/0.030/0.060 (MSWD=0.54)	48.219 ± 0.021/0.030/0.060 (MSWD=0.34)	0.004
NC-MPE-088	48.205 ± 0.020/0.030/0.060 (MSWD=0.42)	48.205 ± 0.020/0.030/0.060 (MSWD=0.44)	0.000
NC-MPE-583	48.185 ± 0.016/0.027/0.058 (MSWD=1.27)	48.185 ± 0.016/0.027/0.058 (MSWD=1.29)	0.000
NC-MPE-450	48.146 ± 0.018/0.028/0.059 (MSWD=1.08)	48.147 ± 0.018/0.028/0.059 (MSWD=1.09)	0.001
NC-MPE-523	48.144 ± 0.017/0.027/0.058 (MSWD=1.33)	48.146 ± 0.017/0.027/0.058 (MSWD=1.35)	0.002
NC-MPE-086	48.139 ± 0.014/0.025/0.057 (MSWD=1.44)	48.136 ± 0.014/0.026/0.057 (MSWD=1.19)	0.003
NC-MPE-510	48.129 ± 0.016/0.026/0.058 (MSWD=1.26)	48.129 ± 0.016/0.026/0.058 (MSWD=1.24)	0.000
NC-MPE-499	48.120 ± 0.017/0.027/0.058 (MSWD=0.50)	48.121 ± 0.017/0.027/0.058 (MSWD=0.50)	0.001
NC-MPE-200	48.045 ± 0.034/0.041/0.066 (MSWD=1.33)	48.041 ± 0.034/0.041/0.066 (MSWD=1.32)	0.004
NC-MPE-565A	47.799 ± 0.018/0.028/0.058 (MSWD=1.38)	47.796 ± 0.018/0.028/0.058 (MSWD=1.30)	0.003
NC-MPE-485	47.729 ± 0.015/0.026/0.057 (MSWD=0.64)	47.727 ± 0.015/0.026/0.057 (MSWD=0.53)	0.002
NC-MPE-517	47.988 ± 0.052/0.056/0.076 (Max. Age)	47.972 ± 0.053/0.057/0.077 (Max. Age)	0.016

*f_{ThU}=0.138 for granitoids (Stelten et al., 2015) or f_{ThU}=0.33 for the diorite (Rubatto and Hermann, 2007).
†$[Th/U]_{Magma}$= 2.8 ± 1.0 (2σ) for all samples.

TABLE DR6: MAGMA EMPLACEMENT RATES IN UPPER CRUSTAL GRANITOID PLUTONS

Intrusive Complex	Intrusion Depth (km)	Area (km^2)	Vertical Relief (km)	Volume (km^3)	Oldest Date (Ma)*	Youngest Date (Ma)*	Emplacement Rate (km^3/yr) †	References
1) Lago della Vacca pluton	12	9.7	1.0	10	42.07 ± 0.04	41.76 ± 0.03	0.00003	John and Blundy (1993), Schoene et al. (2012)
2) Lamarck granodiorite	8-12	600	3.0	1800	94.26 ± 0.17	90.9 ± 0.2	0.00053	Davis et al. (2012)
3) Mt. Givens granodiorite	9	1500	3.0	4500	97.92 ± 0.06	90.87 ± 0.05	0.00133	McNulty et al. (2002), Frazer et al. (2014)
4) Mt. Princeton batholith	3	450	1.5	675	35.80 ± 0.09	35.37 ± 0.10	0.00153	Mills and Coleman (2013)
5) Mt. Stuart batholith (Old Domain)	6-12	194	2.5	485	95.88 ± 0.03	94.25 ± 0.14	0.00030	Matzel et al. (2006)
6) Mt. Stuart batholith (Young Domain)	6-12	208	2.5	520	90.92 ± 0.05	90.78 ± 0.08	0.00316	Matzel et al. (2006)
7) Muir intrusive suite	8-12	1700	3.0	5100	95.45 ± 0.32	83.5 ± 0.5§	0.00043	Davis et al. (2012)
8) Rio Honda pluton	< 5	90	1.2	108	22.98 ± 0.09	22.59 ± 0.06	0.00027	Tappa et al. (2011)
9) Torres del Paine complex	2-3	80	2.0	88	12.593 ± 0.009	12.431 ± 0.006	0.00054	Leuthold et al. (2012)
10) Tuolumne intrusive suite	3-9	1200	2.0	2400	94.4 ± 0.3	85.1 ± 0.9	0.00026	Coleman et al. (2004), Memeti et al. (2010)

* ID-TIMS $^{206}Pb/^{238}U$ zircon dates

† Emplacement rates were calculated using the mode of Monte Carlo simulations with 10^7 iterations

§ The uncertainty for this sample was not reported in Davis et al. (2011), we apply a conservative estimate of 0.5 Ma

Figure DR1

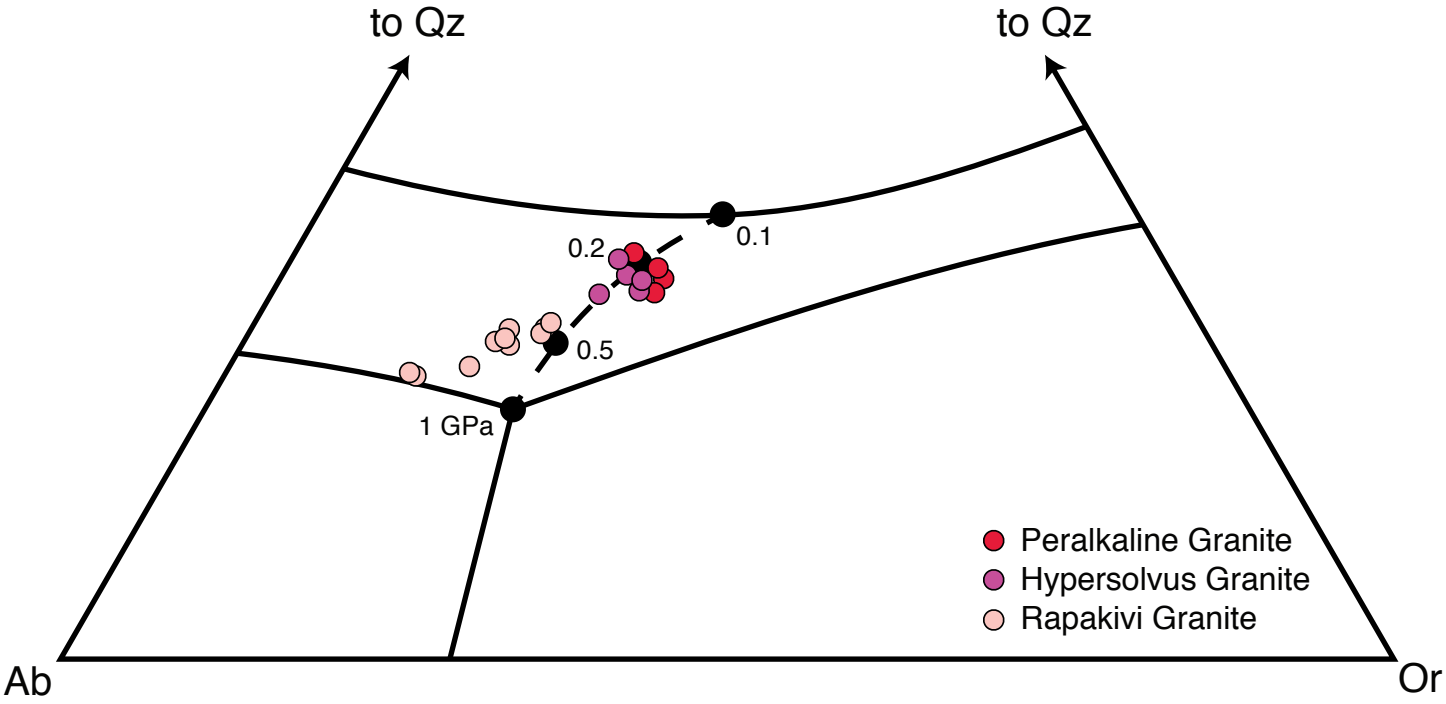

Figure DR2

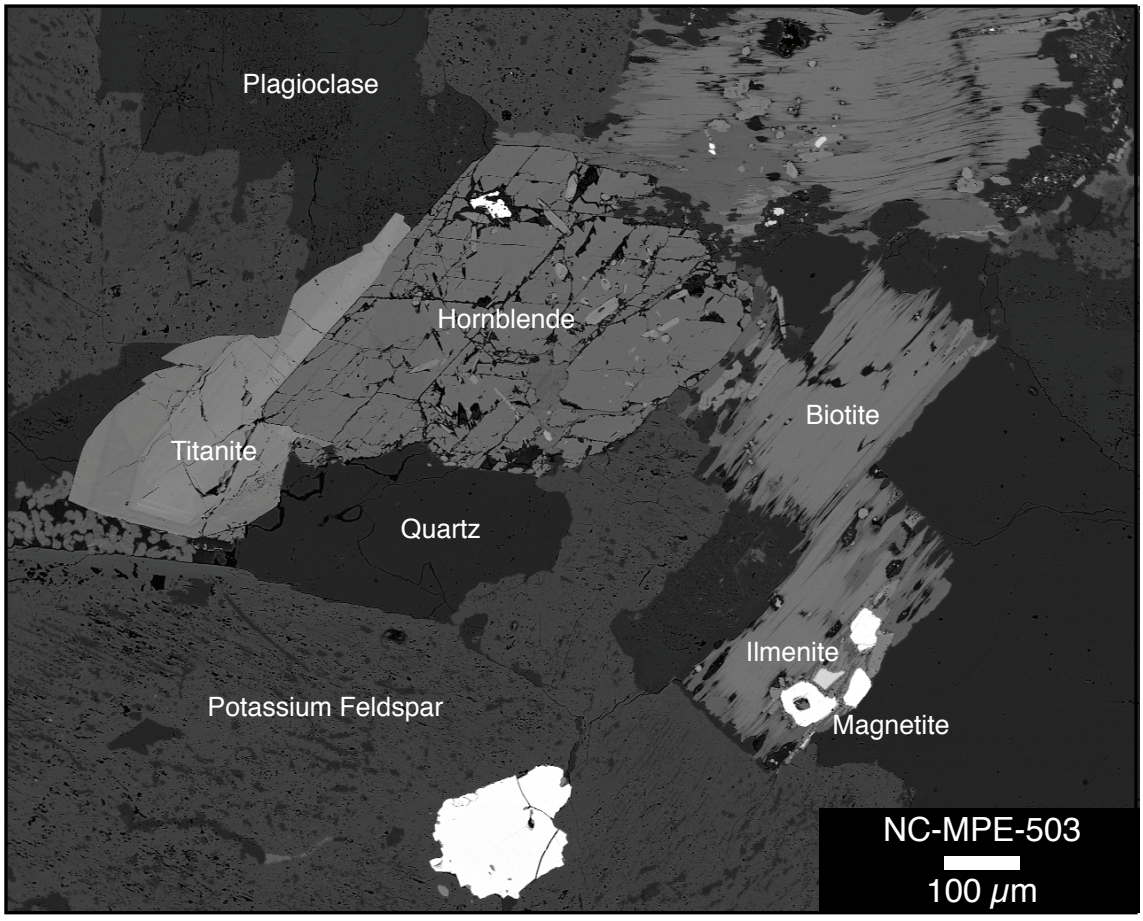

Figure DR3

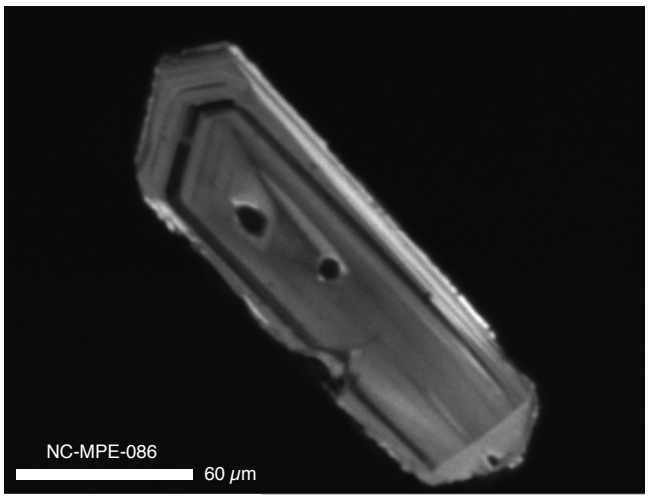

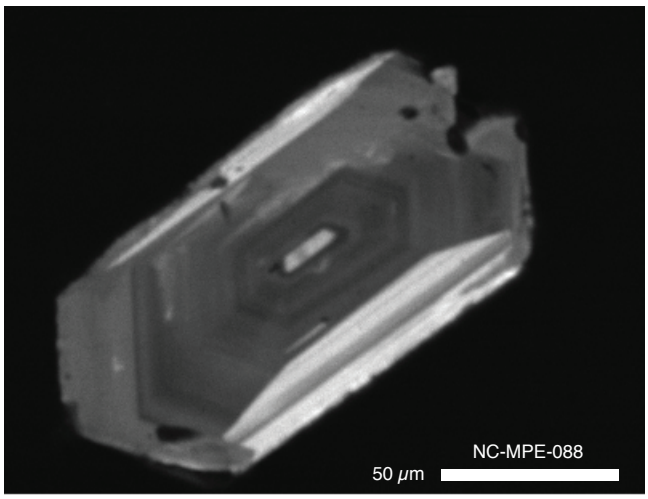

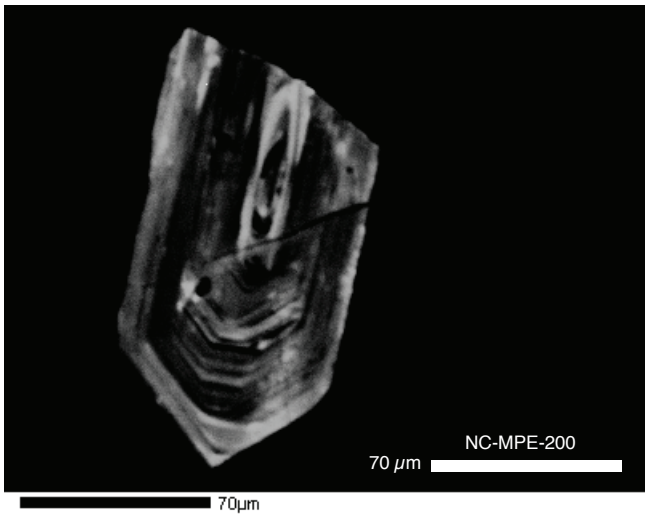

CL NC-MPE-200 z19

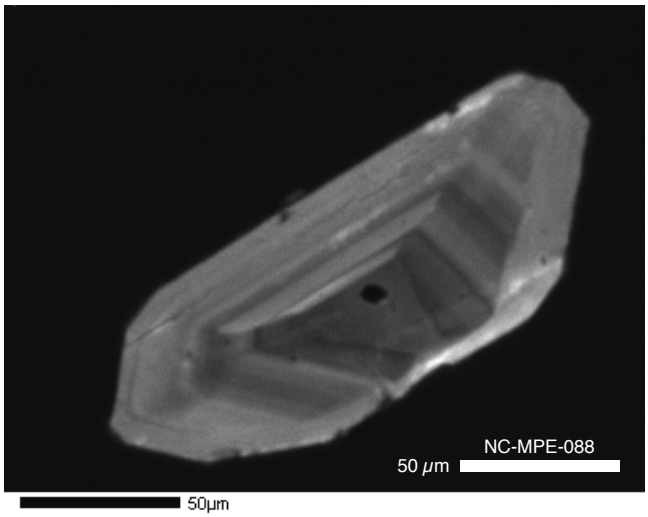

CL NC-MPE-088 z17

Figure DR4

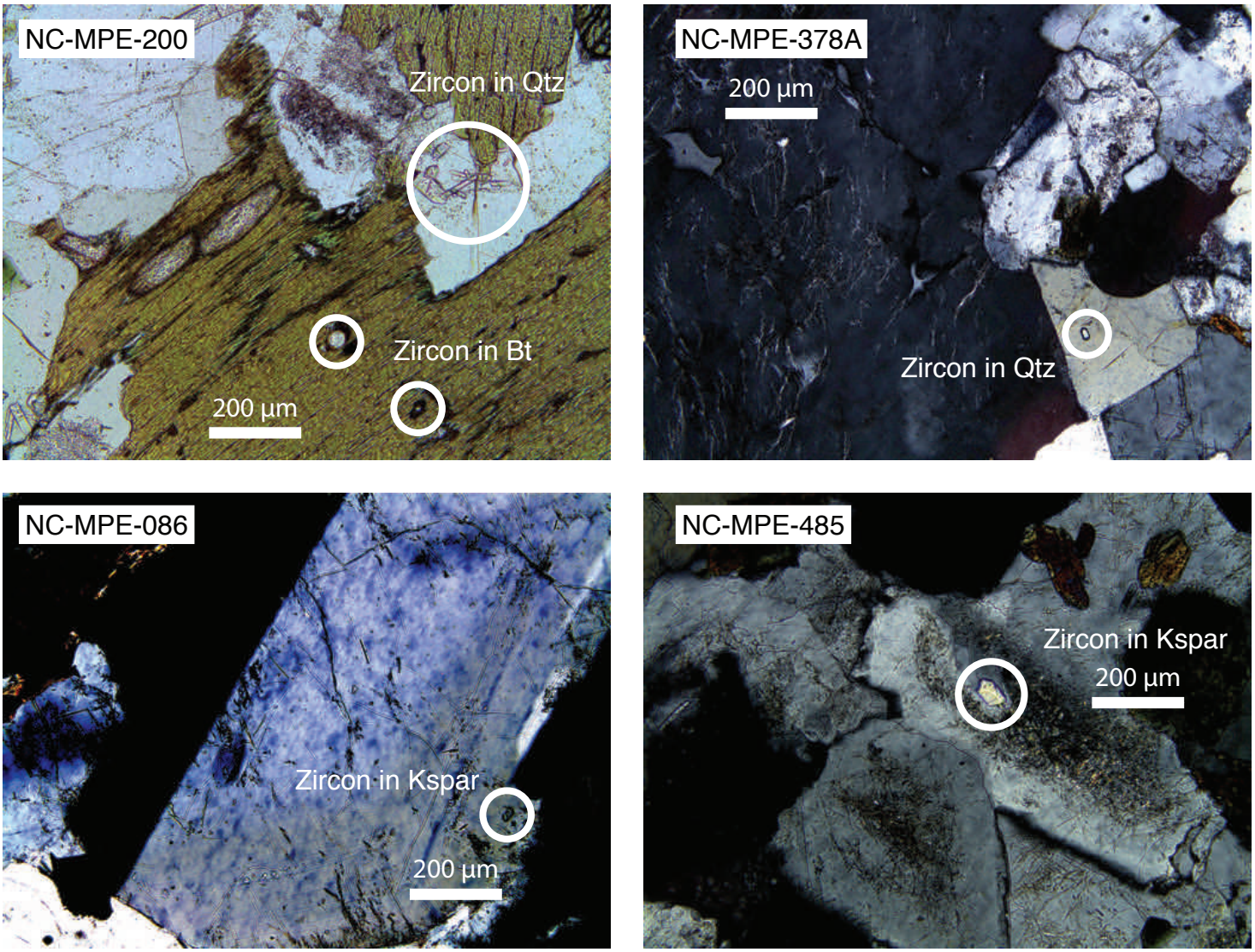

Figure DR5

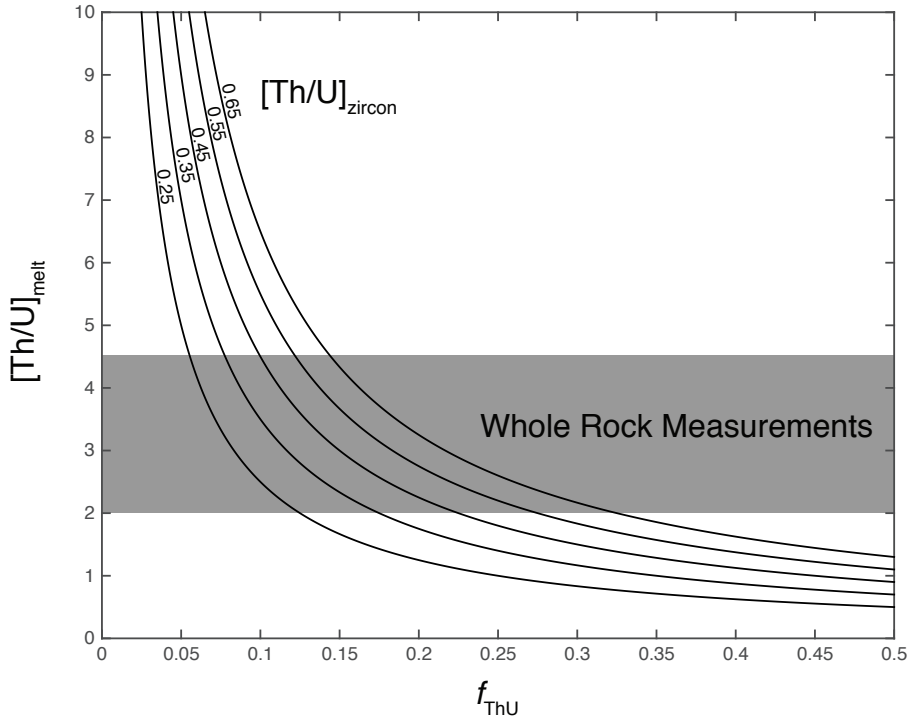

Figure DR6

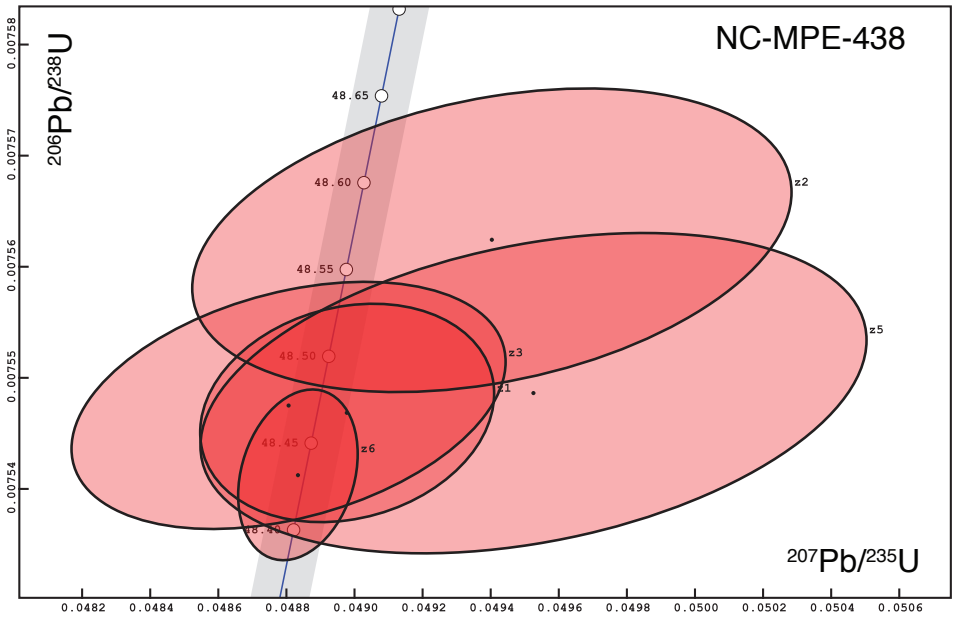
NC-MPE-438
206Pb/238U
207Pb/235U
48.65
48.60
48.55
48.50
48.45
48.40
z1
z2
z3
z5
z6
0.00758
0.00757
0.00756
0.00755
0.00754
0.0482
0.0484
0.0486
0.0488
0.0490
0.0492
0.0494
0.0496
0.0498
0.0500
0.0502
0.0504
0.0506

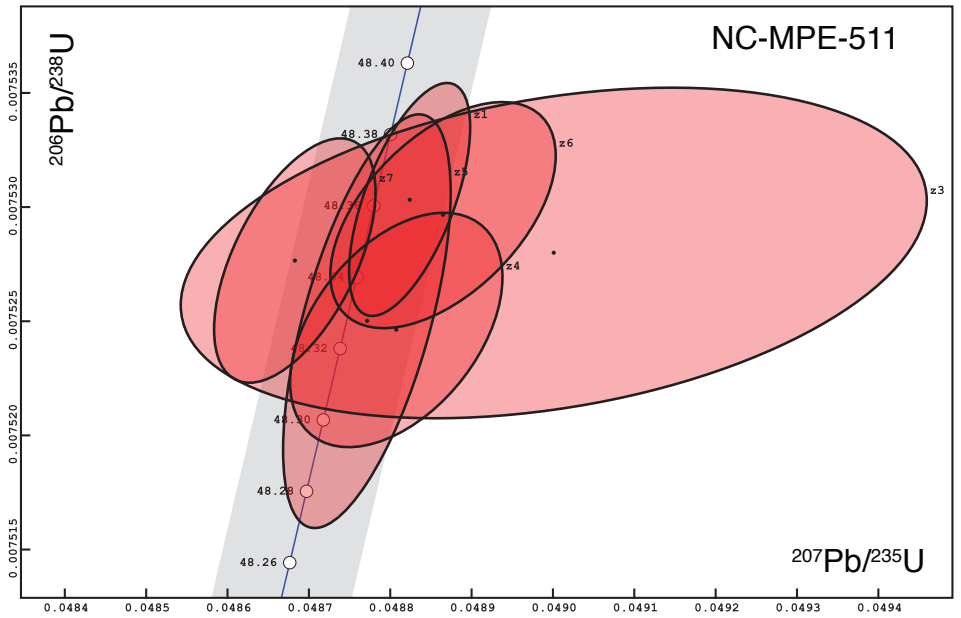
NC-MPE-511
206Pb/238U
207Pb/235U
48.40
48.38
48.30
48.28
48.26
z1
z3
z4
z6
z7
0.007535
0.007530
0.007525
0.007520
0.007515
0.0484
0.0485
0.0486
0.0487
0.0488
0.0489
0.0490
0.0491
0.0492
0.0493
0.0494

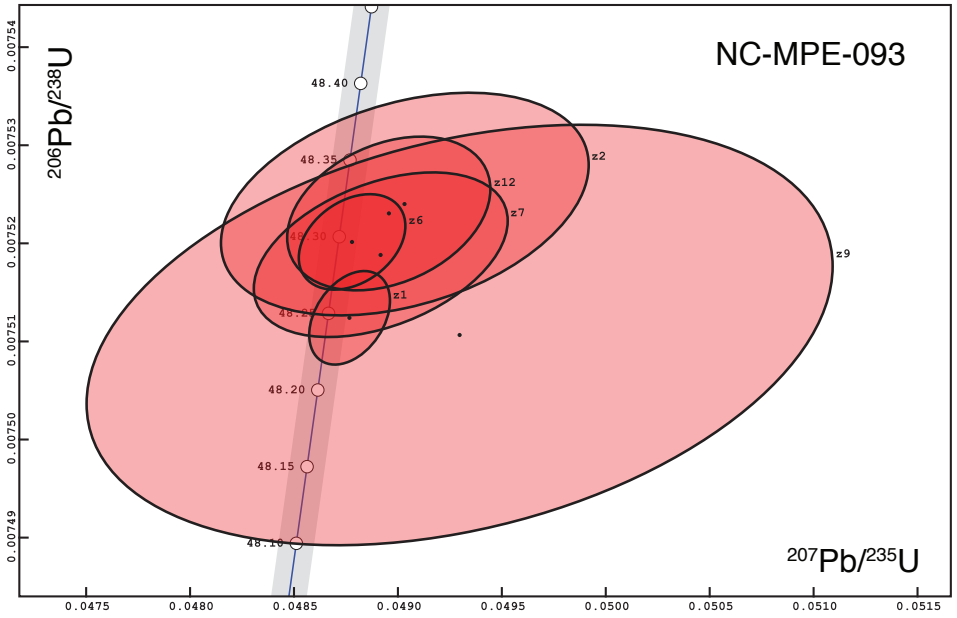
NC-MPE-093
206Pb/238U
207Pb/235U
48.40
48.35
48.30
48.25
48.20
48.15
48.10
z1
z2
z6
z7
z9
z12
0.00754
0.00753
0.00752
0.00751
0.00750
0.00749
0.0475
0.0480
0.0485
0.0490
0.0495
0.0500
0.0505
0.0510
0.0515

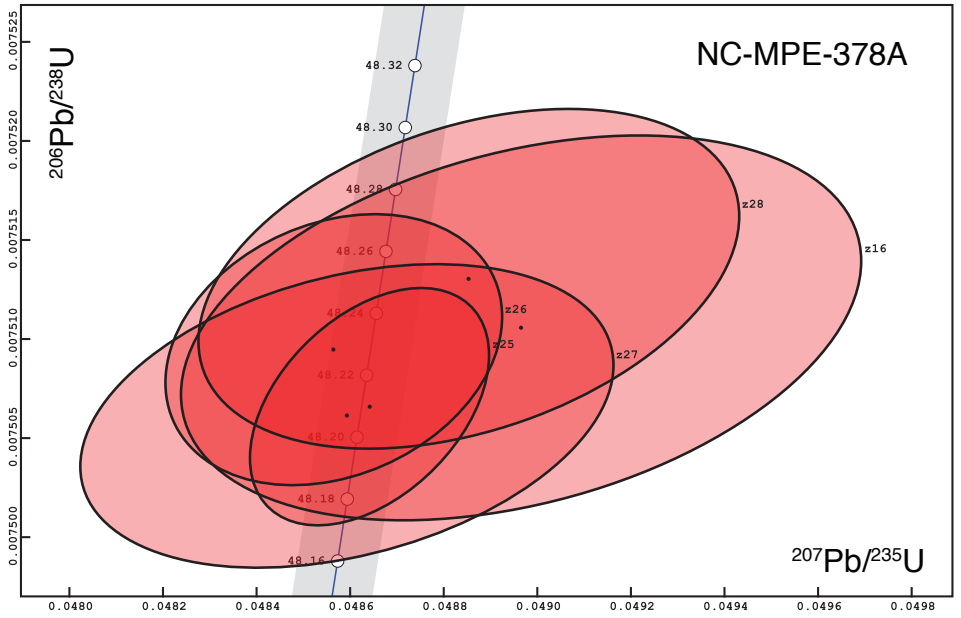
NC-MPE-378A
206Pb/238U
207Pb/235U
48.32
48.30
48.28
48.26
48.24
48.22
48.20
48.18
48.16
z16
z25
z26
z27
z28
0.007525
0.007520
0.007515
0.007510
0.007505
0.007500
0.0480
0.0482
0.0484
0.0486
0.0488
0.0490
0.0492
0.0494
0.0496
0.0498

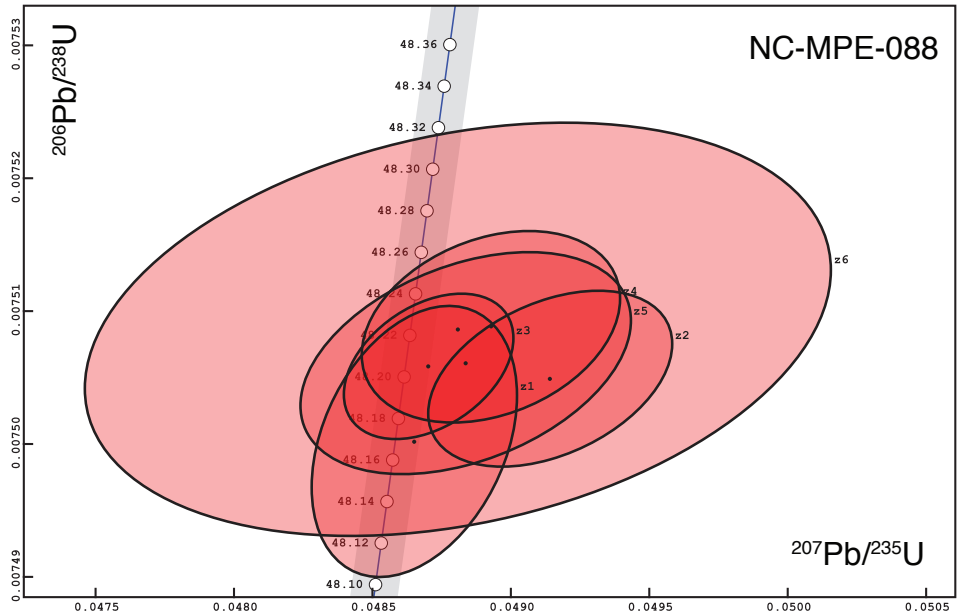
NC-MPE-088
$^{206}Pb/^{238}U$
$^{207}Pb/^{235}U$
48.36
48.34
48.32
48.30
48.28
48.26
48.24
48.22
48.20
48.18
48.16
48.14
48.12
48.10
z1
z2
z3
z4
z5
z6
0.00753
0.00752
0.00751
0.00750
0.00749
0.0475
0.0480
0.0485
0.0490
0.0495
0.0500
0.0505

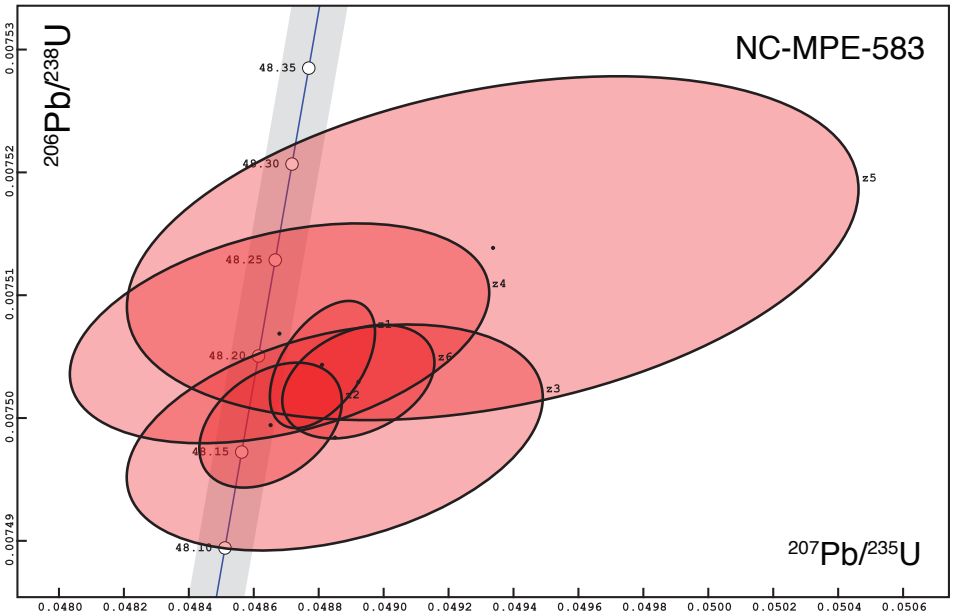
NC-MPE-583
$^{206}Pb/^{238}U$
$^{207}Pb/^{235}U$
48.35
48.30
48.25
48.20
48.15
48.10
z1
z2
z3
z4
z5
z6
0.00753
0.00752
0.00751
0.00750
0.00749
0.0480
0.0482
0.0484
0.0486
0.0488
0.0490
0.0492
0.0494
0.0496
0.0498
0.0500
0.0502
0.0504
0.0506

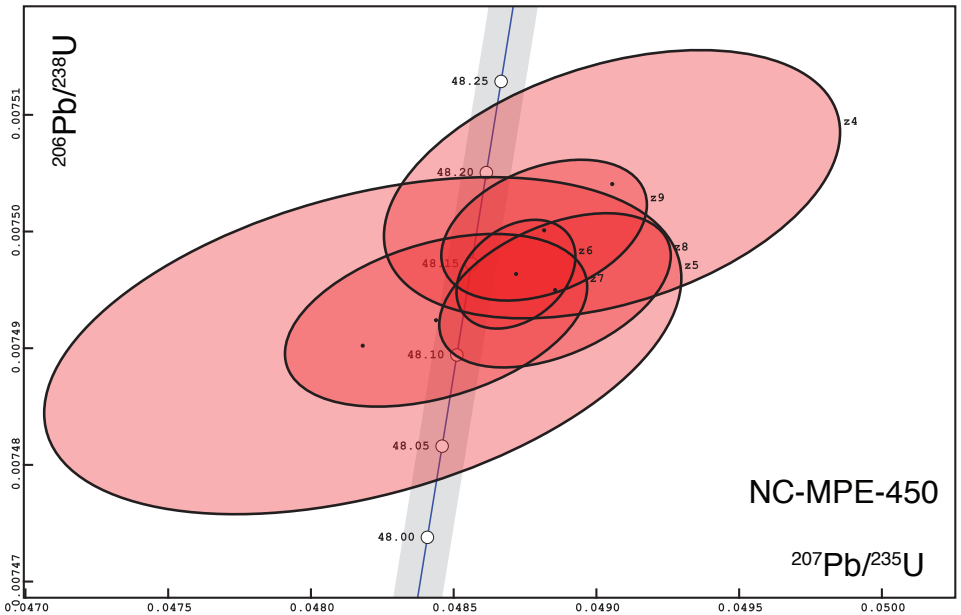
NC-MPE-450
$^{206}Pb/^{238}U$
$^{207}Pb/^{235}U$
48.25
48.20
48.15
48.10
48.05
48.00
z4
z5
z6
z7
z8
z9
0.00751
0.00750
0.00749
0.00748
0.00747
0.0470
0.0475
0.0480
0.0485
0.0490
0.0495
0.0500

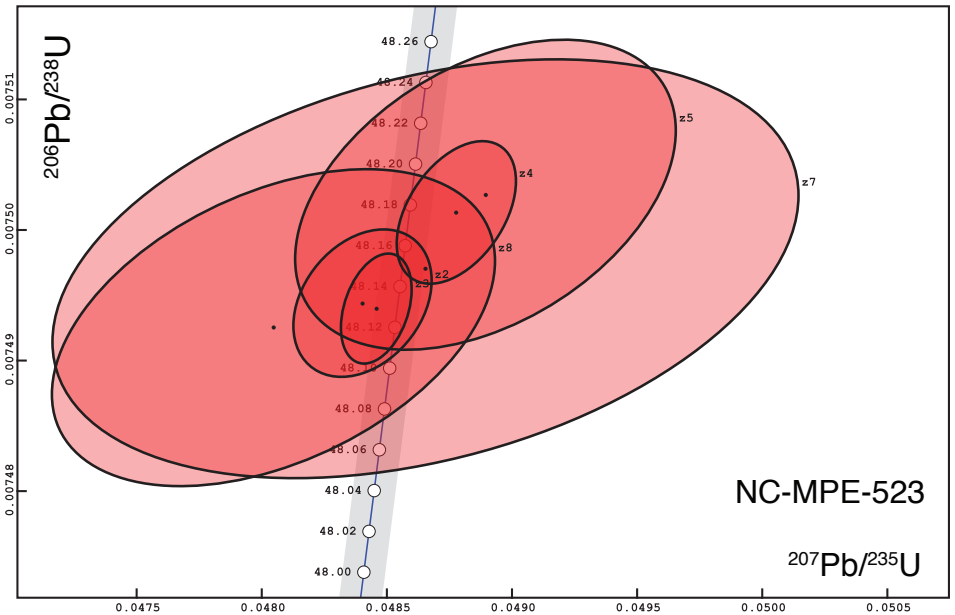
NC-MPE-523
$^{206}Pb/^{238}U$
$^{207}Pb/^{235}U$
48.26
48.24
48.22
48.20
48.18
48.16
48.14
48.12
48.10
48.08
48.06
48.04
48.02
48.00
z2
z3
z4
z5
z7
z8
0.00751
0.00750
0.00749
0.00748
0.0475
0.0480
0.0485
0.0490
0.0495
0.0500
0.0505

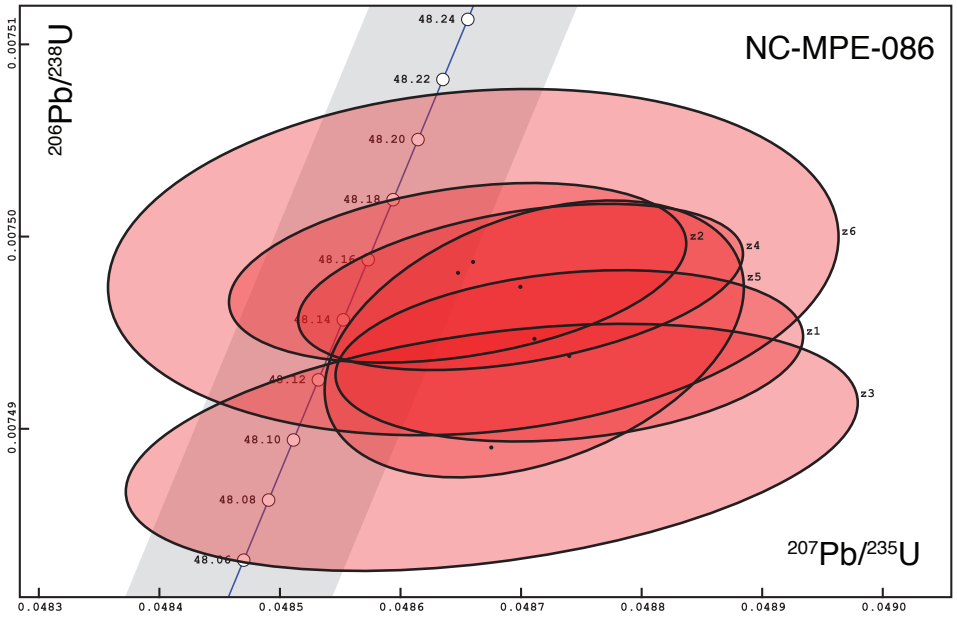
NC-MPE-086
206Pb/238U
207Pb/235U
48.24
48.22
48.20
48.18
48.16
48.14
48.12
48.10
48.08
48.06
z1
z2
z3
z4
z5
z6
0.00751
0.00750
0.00749
0.0483
0.0484
0.0485
0.0486
0.0487
0.0488
0.0489
0.0490

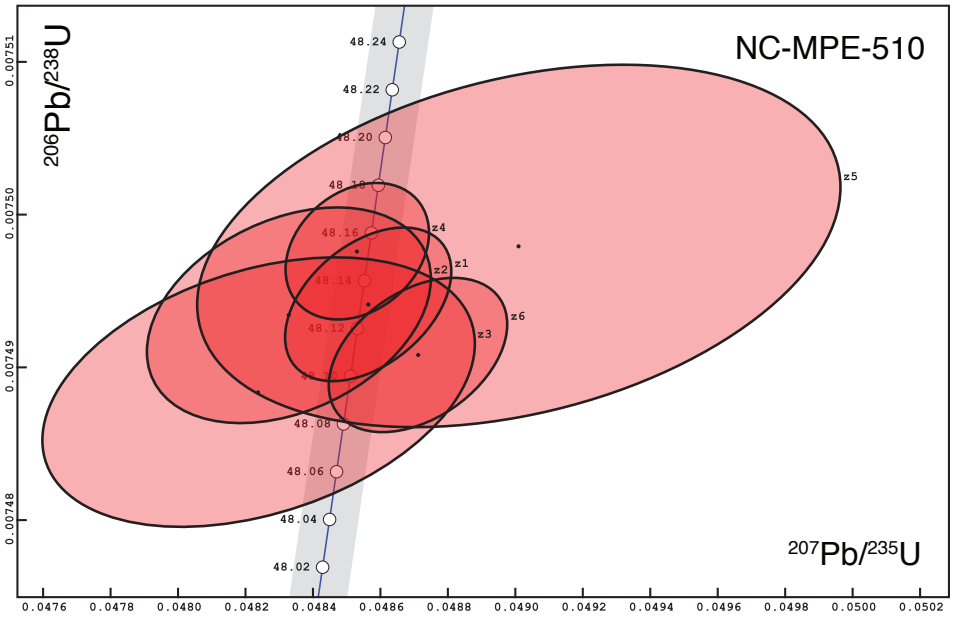
NC-MPE-510
206Pb/238U
207Pb/235U
48.24
48.22
48.20
48.18
48.16
48.14
48.12
48.08
48.06
48.04
48.02
z1
z2
z3
z4
z5
z6
0.00751
0.00750
0.00749
0.00748
0.0476
0.0478
0.0480
0.0482
0.0484
0.0486
0.0488
0.0490
0.0492
0.0494
0.0496
0.0498
0.0500
0.0502

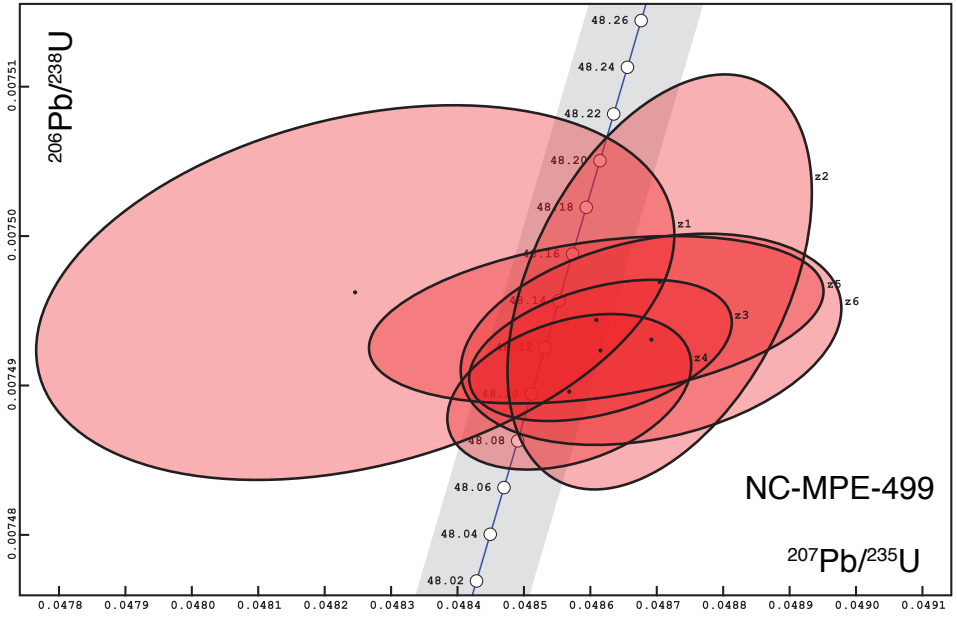
NC-MPE-499
206Pb/238U
207Pb/235U
48.26
48.24
48.22
48.20
48.18
48.16
48.08
48.06
48.04
48.02
z1
z2
z3
z4
z6
z6
0.00751
0.00750
0.00749
0.00748
0.0478
0.0479
0.0480
0.0481
0.0482
0.0483
0.0484
0.0485
0.0486
0.0487
0.0488
0.0489
0.0490
0.0491

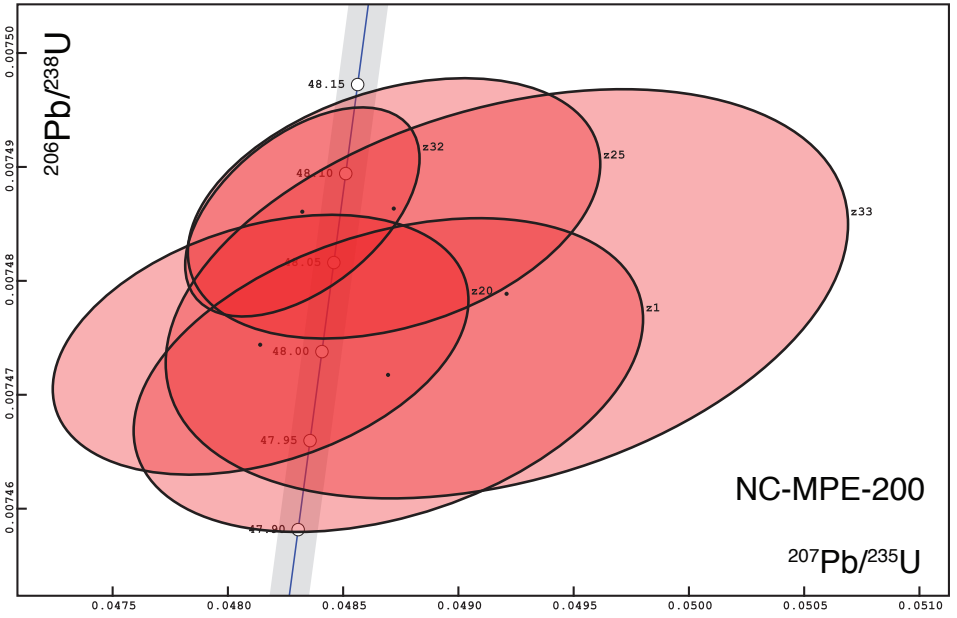
NC-MPE-200
206Pb/238U
207Pb/235U
48.15
48.10
48.00
47.95
47.90
z1
z20
z25
z32
z33
0.00750
0.00749
0.00748
0.00747
0.00746
0.0475
0.0480
0.0485
0.0490
0.0495
0.0500
0.0505
0.0510

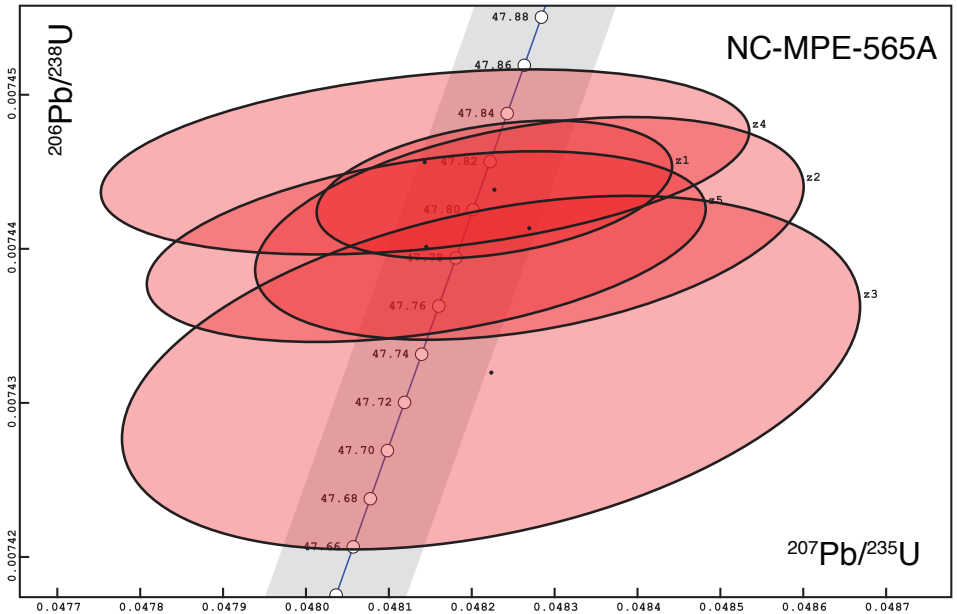
NC-MPE-565A
206Pb/238U
207Pb/235U
47.88
47.86
47.84
47.82
47.80
47.78
47.76
47.74
47.72
47.70
47.68
47.66
z1
z2
z3
z4
z5
0.00745
0.00744
0.00743
0.00742
0.0477
0.0478
0.0479
0.0480
0.0481
0.0482
0.0483
0.0484
0.0485
0.0486
0.0487

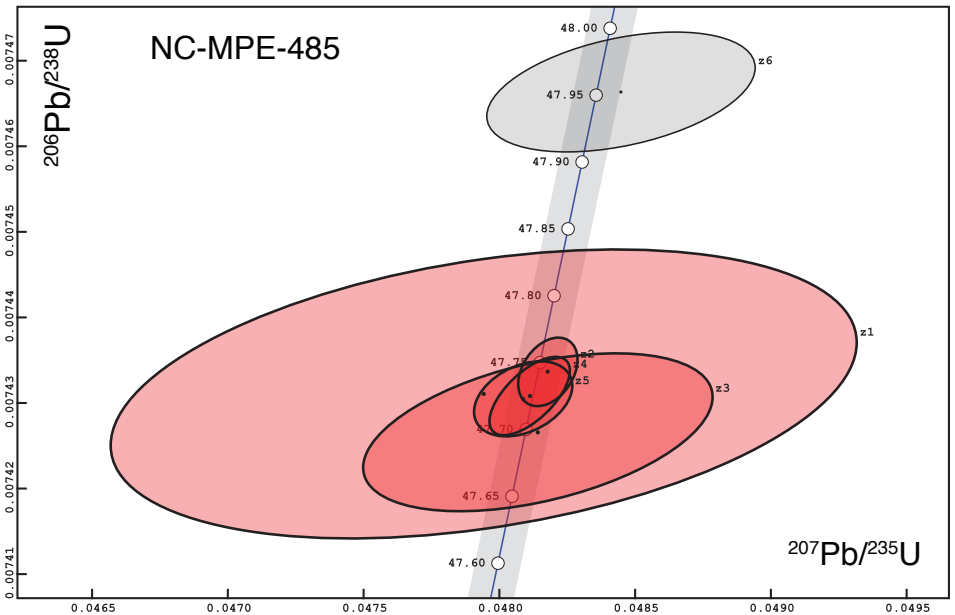
NC-MPE-485
206Pb/238U
207Pb/235U
48.00
47.95
47.90
47.85
47.80
47.75
47.70
47.65
47.60
z1
z2
z3
z4
z5
z6
0.00747
0.00746
0.00745
0.00744
0.00743
0.00742
0.00741
0.0465
0.0470
0.0475
0.0480
0.0485
0.0490
0.0495

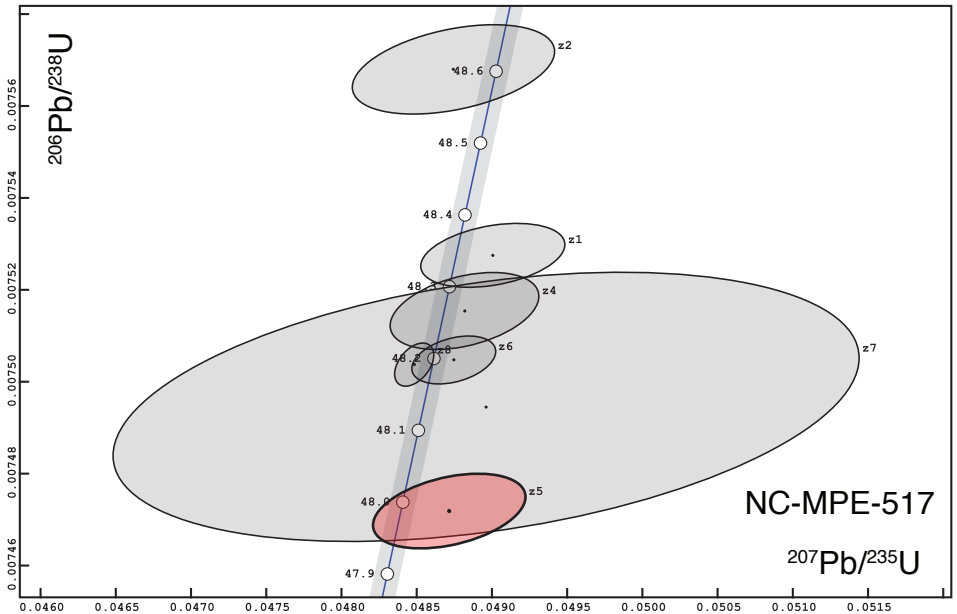
NC-MPE-517
206Pb/238U
207Pb/235U
48.6
48.5
48.4
48.3
48.2
48.1
48.0
47.9
z1
z2
z4
z5
z6
z7
0.00756
0.00754
0.00752
0.00750
0.00748
0.00746
0.0460
0.0465
0.0470
0.0475
0.0480
0.0485
0.0490
0.0495
0.0500
0.0505
0.0510
0.0515

Figure DR7

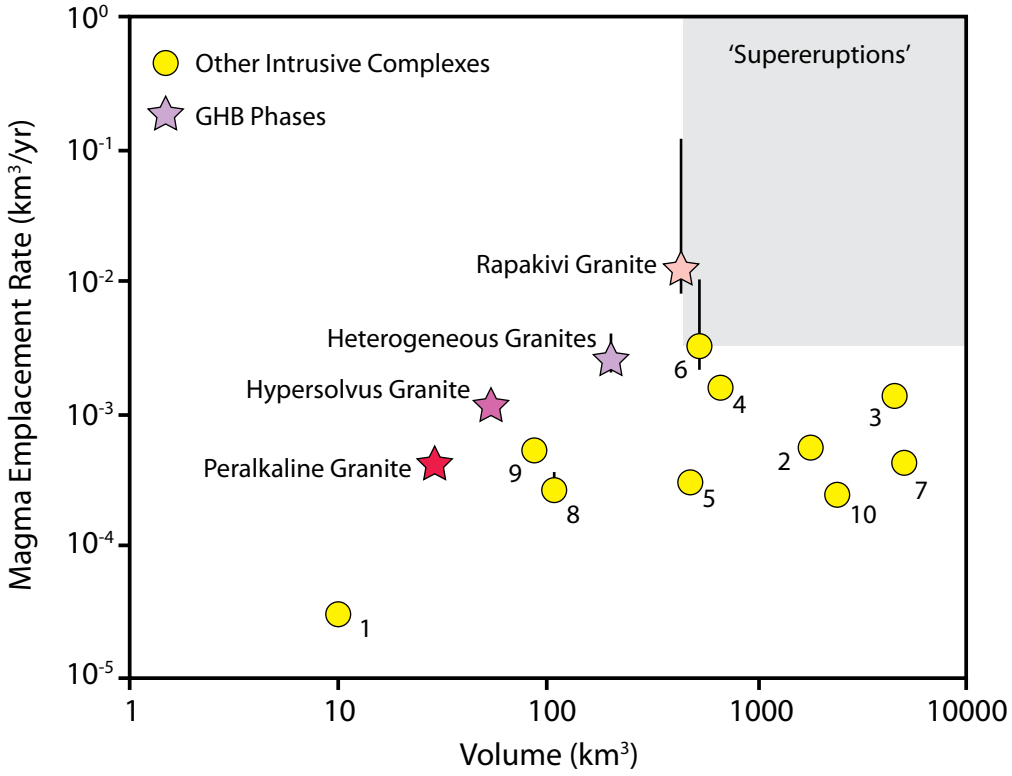
Other Intrusive Complexes
GHB Phases
'Supereruptions'
Rapakivi Granite
Heterogeneous Granites
Hypersolvus Granite
Peralkaline Granite
1
2
3
4
5
6
7
8
9
10
Magma Emplacement Rate (km³/yr)
Volume (km³)
10⁰
10⁻¹
10⁻²
10⁻³
10⁻⁴
10⁻⁵
1
10
100
1000
10000